Progress in Oceanography 241 (2026) 103659

Contents lists available at ScienceDirect

Progress in Oceanography

journal homepage: www.elsevier.com/locate/pocean

Surface water pCO_2 and air-sea fluxes in the southeastern coast of Mainland China: Synthesis of a 22-year dataset of field observation

Dezhi Bu [a], Xianghui Guo [a,b,c,*], Weidong Zhai [d], Yi Xu [a], Minhan Dai [a]

[a] State Key Laboratory of Marine Environmental Science, College of Ocean and Earth Sciences, Xiamen University, Xiamen 361102, China
[b] Fujian Provincial Key Laboratory for Coastal Ecology and Environmental Studies, Xiamen University, Xiamen 361102, China
[c] Dongshan Swire Marine Station, Xiamen University, Dongshan 363499, China
[d] Frontier Research Center, Southern Marine Science and Engineering Guangdong Laboratory (Zhuhai), Zhuhai 519082, China

ARTICLE INFO

Keywords:
Southeastern coast of Mainland China
Surface water pCO_2
Air-sea CO_2 flux
Seasonal variability
Spatial variability

ABSTRACT

Air-sea CO_2 flux in marginal sea is an important component of the global ocean carbon cycle. Located between the East China Sea and the northern South China Sea shelves which are both CO_2 sinks, the southeastern coast of Mainland China has large potential of CO_2 sequestration, but studies on air-sea CO_2 fluxes in this region are very limited. Surface water CO_2 partial pressure (pCO_2) and auxiliary parameters from 51 cruises conducted in 2001–2022 were integrated to estimate the air-sea CO_2 fluxes. Surface water pCO_2 exhibited conspicuous spatial and temporal variabilities. The lowest pCO_2 occurred in winter (349 ± 20 μatm), gradually increased in spring (357 ± 21 μatm) and summer (371 ± 35 μatm), and reached a peak in fall (392 ± 27 μatm). Surface water pCO_2 was primarily modulated by vertical mixing and cooling during cold seasons, and by coastal upwelling and biological CO_2 uptake in warm seasons. Vertical water mixing and temperature effect induced highest pCO_2 in fall. Air-sea CO_2 fluxes also exhibited strong seasonal variations. The study area acts as a moderate to strong CO_2 sinks of 9.4 ± 5.5 and 3.7 ± 3.9 mmol m^{-2} d^{-1} in winter and spring, respectively, and a CO_2 source of 3.8 ± 7.0 mmol m^{-2} d^{-1} in fall. In summer, the surface water CO_2 is near equilibrium with the atmosphere with an air-sea CO_2 flux of −0.6 ± 2.8 mmol m^{-2} d^{-1}. The annual average air-sea CO_2 fluxes is −2.6 ± 6.8 mmol m^{-2} d^{-1}, indicating the study area acting as a weak to moderate sink annually. pCO_2 difference between the surface water and the atmosphere is the main factor regulating the seasonal variations of air-sea CO_2 flux, and wind speed also played an important role, enhancing CO_2 sink in winter.

1. Introduction

Carbon cycle in marginal seas, connecting the land and the open ocean, is an important component of the global carbon cycle (Cai, 2011; Thomas et al., 2004; Peter et al., 2025). Studies have implied that the global marginal seas contribute10%-25 % of the annual global ocean CO_2 sequestration, with only 7% of the surface area (Borges et al., 2005; Takahashi et al., 2009; Laruelle et al., 2010; Dai et al., 2013). However, estimates of air-sea CO_2 fluxes in marginal seas still have large uncertainties (Dai et al., 2022; Borges and Frankignoulle, 1999; Hales et al., 2005; Evans et al., 2011). With the effort on the air-sea CO_2 flux studies over the past decades, estimates of global marginal sea air-sea CO_2 fluxes have converged to around 0.2 to 0.5 Pg Cyr^{-1} (Borges et al., 2005; Cai et al., 2006; Chen et al., 2013; Dai et al.,2013; Laruelle et al., 2018). Understanding regional air-sea CO_2 fluxes and their controls are important because it not only affects the marginal sea carbon fluxes estimation but also improves our capability of modelling the coastal ocean carbon cycle. However, the physical-biogeochemical coupling processes in the marginal seas are very complex, making the accurate estimation of air-sea CO_2 fluxes and revealing the controlling mechanisms very challenging (Hales et al., 2005).

The marginal seas exhibit unique physical, chemical, and biological characteristics, with strong ocean–atmosphere interactions. Generally, the marginal seas are significantly influenced by terrestrial and anthropogenic activities (Dai et al., 2022). The strong physical and biogeochemical processes in the more dynamic marginal seas add more complex to the carbon cycle and the air-sea CO_2 exchange. Additionally, coastal upwelling may bring CO_2-repleted and nutrient-rich deep waters

* Corresponding author at: State Key Laboratory of Marine Environmental Science, College of Ocean and Earth Sciences, Xiamen University, Xiamen 361102, China.
E-mail address: xhguo@xmu.edu.cn (X. Guo).

https://doi.org/10.1016/j.pocean.2025.103659
Received 11 November 2025; Accepted 20 December 2025
Available online 22 December 2025

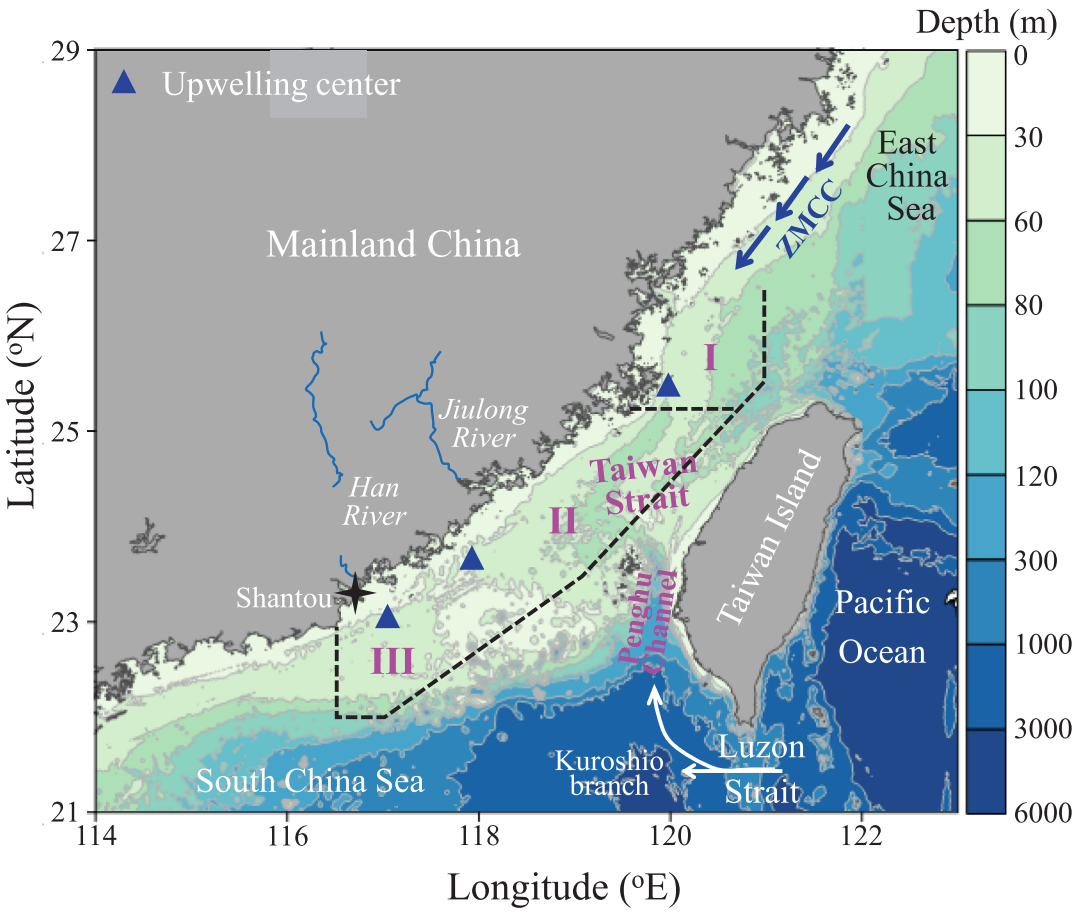

Fig. 1. Map of the southeastern coast of Mainland China. ZMCC is the Zhejiang-Fujian (Min) Coastal Current under the influence of the northeastern monsoon. The three sub-regions circled by dashed lines marked with I, II and III are the three domains. The triangles are the upwelling centers during summer. The star marks the location of the city Shanwei.

to the surface water, further complicating the CO_2 sink/source of the marginal seas (Hales et al., 2005).

Mainland China is enclosed by the Bohai, Yellow Sea, East China Sea and South China Sea. Studies on the Yellow Sea, East China Sea and South China Sea are relatively abundant (Zhai et al., 2005; Shim et al., 2007; Chou et al., 2009; Zhai et al., 2009; Chou et al., 2011; Tseng et al., 2011; Kim et al., 2013; Zhai et al., 2013; Guo et al., 2015; Li et al., 2020; Yang et al., 2021). More than twenty years ago, preliminary studies have showed that the East China Sea acts as a sink of the atmospheric CO_2 (Tsunogai et al., 1997; 1999). After the effort of more than two decades, the East China Sea have been proved to be a strong CO_2 sink annually (Tseng et al., 2011; Guo et al., 2015). Zhai et al. (2013) and Li et al. (2020) provided a comprehensive assessment of the air-sea CO_2 fluxes in the South China Sea based on large datasets of several decades of surveys conducted during 2000–2018, and they indicated that the northern South China Sea shelf is a moderate CO_2 sink annually. The southwestern coast of Mainland China links the two regions of CO_2 sink, and it has a large CO_2 sink potential. However, studies on the air-sea CO_2 fluxes in this area are very limited.

In this study, a large dataset of 51 cruises collected in the southeastern coast of Mainland China from 2001 to 2022 were integrated. We aim to reveal (1) the seasonal and spatial variations of surface water pCO_2 and air-sea CO_2 fluxes, (2) intra-seasonal variability of CO_2 sinks/sources, (3) the major controlling factors in each physically and biogeochemically distinct regions of the southeastern coast of Mainland China.

2. Materials and methods

2.1. Study area

The southeastern coastal region of Mainland China is a strip-shaped polygon with a northeast-southwest orientation along the coastline (Fig. 1). The study area extends from the northeast of the Pearl River estuary (116.5°E, 22.0°N) to the Fujian-Zhejiang coast (121.0°E, 26.5°N) through the Taiwan Strait. The topography of the southeastern Mainland China coast is complex, with a series of underwater sandbars in the middle of the Taiwan Strait forming the Taiwan Shoal, where the water depth is less than 50 m, and multiple oceanic fronts exist. The 100 m isobath line extends northward into the strait beyond the Taiwan Shoal, forming the Penghu Channel. To the west of the shoal, there is another channel where an upwelling current forms in summer, converging with the diluted water from the Han River (Li et al., 2000).

Located in the East Asian monsoon zone, northeast monsoon prevails from October to April of the following year with high wind speeds, while southwest monsoon prevails from June to August with relatively lower wind speeds. Additionally, influenced by topography, the waters in the study area, especially in the Taiwan Strait, present a trumpet-shaped "wider in the south, narrower in the north" configuration. The unique topography induces a "strait channel effect" on the airflow passing through the Taiwan Strait, resulting in higher average wind speeds within the Taiwan Strait in winter compared to areas outside the strait (Chen, 2011).

The water in the study area is mainly influenced by the dilution waters from the Han River, the Pearl River and other local rivers from

Table 1
Summary of the cruise information.

Season	Survey period	R/V	Sampler configuration	Data source
Winter	Dec. 22–23, 2006	Dongfanghong 2	Modified from Jiang et al. (2008) + Licor 7000	(Zhai et al., 2013; Li et al., 2020)
	Dec. 27–30, 2008	Dongfanghong 2	GO-8050 + Licor 7000	(Li et al., 2020)
	Dec. 3, 26 and 27, 2022	Jiageng	GO-8050 + Picarro 2301	This study
	Jan. 8–11, 2009	Dongfanghong 2	GO-8050 + Licor 7000	(Li et al., 2020)
	Jan. 1–5 and 23–31, 2010	Dongfanghong 2	GO-8050 + Licor 7000	(Li et al., 2020)
	Jan. 14, 2018	Jiageng	Modified from Jiang et al. (2008) + Picarro 2301	(Li et al., 2020)
	Feb. 10–11, 2004	Yanping 2	Modified from Zhai et al. (2005) + Licor 7000	(Zhai et al., 2013; Jo et al., 2012; Li et al., 2020)
	Feb. 1–3, 2010	Dongfanghong 2	GO-8050 + Licor 7000	(Li et al., 2020)
	Feb. 3–4, 2018	Jiageng	Modified from Jiang et al. (2008) + Picarro 2301	(Li et al., 2020)
Spring	Mar. 1–6, 2004	Yanping 2	Modified from Zhai et al. (2005) + Licor 7000	(Zhai et al., 2013; Jo et al., 2012; Li et al., 2020)
	Mar. 31, 2009	Dongfanghong 2	GO-8050 + Licor 7000	(Li et al., 2020)
	Apr. 10 and 25, 2005	Dongfanghong 2	Modified from Zhai et al. (2005) + Licor 6252	(Zhai et al., 2013; Li et al., 2020)
	Apr. 21–28, 2008	Dongfanghong 2	GO-8050 + Licor 7000	(Zhai et al., 2013; Li et al., 2020)
	Apr. 4–6, 14 and 16, 2009	Dongfanghong 2	GO-8050 + Licor 7000	(Li et al., 2020)
	Apr. 30, 2011	Dongfanghong 2	GO-8050 + Licor 7000	(Li et al., 2020)
	Apr. 9–14, 2022	Jiageng	GO-8050 + Picarro 2301	This study
	May 1–5 and 23–31, 2011	Dongfanghong 2	GO-8050 + Licor 7000	(Li et al., 2020)
	May 15–17, 2016	Dongfanghong 2	Modified from Jiang et al. (2008) + Licor 7000	(Li et al., 2020)
	May 20, 2020	Jiageng	GO-8050 + Picarro 2301	This study
	May 5–6, 2021	Jiageng	GO-8050 + Picarro 2301	This study
Summer	Jun. 1, 2001	Yanping 2	Modified from Zhai et al. (2005) + Licor 6252	(Dai et al., 2008; Li et al., 2020)
	Jun. 4, 5, 12, 16 and 17, 2014	Dongfanghong 2	GO-8050 + Licor 7000	(Li et al., 2020)
	Jun. 4–6, 2016	Dongfanghong 2	Modified from Jiang et al. (2008) + Licor 7000	(Li et al., 2020)
	Jun. 5–6 and 26–27, 2017	Jiageng	Modified from Jiang et al. (2008) + Picarro 2301	(Li et al., 2020)
	Jun. 12–13, 19–20 and 24–27, 2018	Jiageng	GO-8050 + Picarro 2301	This study
	Jun. 1 and 26, 2020	Jiageng	GO-8050 + Picarro 2301	This study
	Jun. 7–9, 2021	Jiageng	GO-8050 + Picarro 2301	This study
	Jul. 22–23, 2004	Yanping 2	Modified from Zhai et al. (2005) + Licor 7000	(Zhai and Dai, 2009; Zhai et al., 2013; Li et al., 2020)
	Jul. 22–24, 2007	Dongfanghong 2	Modified from Jiang et al. (2008) + Licor 7000	(Zhai et al., 2013; Li et al., 2020)
	Jul. 1–12 and 14, 2008	Shiyan 3	Modified from Jiang et al. (2008) + Licor 7000	(Li et al., 2020)
	Jul. 17–18, 2009	Dongfanghong 2	GO-8050 + Licor 7000	(Li et al., 2020)
	Jul. 29–30, 2012	Dongfanghong 2	GO-8050 + Licor 7000	(Li et al., 2020)
	Jul. 17–18, 2014	Dongfanghong 2	GO-8050 + Licor 7000	(Li et al., 2020)
	Jul. 11, 16–29, 2018	Jiageng	GO-8050 + Picarro 2301	This study
	Jul. 2, 10–11 and 25–26, 2019	Jiageng	GO-8050 + Picarro 2301	This study
	Aug. 20–23, 2008	Dongfanghong 2	GO-8050 + Licor 7000	(Li et al., 2020)
	Aug. 15–20, 2009	Dongfanghong 2	GO-8050 + Licor 7000	(Li et al., 2020)
	Aug. 20–21, 2012	Dongfanghong 2	GO-8050 + Licor 7000	(Li et al., 2020)
	Aug. 2–3, 2018	Jiageng	GO-8050 + Picarro 2301	This study
	Aug. 27, 2019	Jiageng	GO-8050 + Picarro 2301	This study
	Aug. 26, 2021	Jiageng	GO-8050 + Picarro 2301	This study
Fall	Sep. 21–22, 2004	Shiyan 3	Modified from Zhai et al. (2005) + Licor 7000	(Zhai et al., 2013; Li et al., 2020)
	Sep. 24–25 and 30, 2006	Kwxue 3	Modified from Jiang et al. (2008) + Licor 7000	(Zhai et al., 2013; Li et al., 2020)
	Sep. 17–18, 2018	Jiageng	GO-8050 + Picarro 2301	This study
	Sep. 1–2 and 29–30, 2020	Jiageng	GO-8050 + Picarro 2301	This study
	Oct. 1 and 14, 2006	Kexue 3	Modified from Jiang et al. (2008) + Licor 7000	(Zhai and Dai, 2009; Zhai et al., 2013; Guo et al., 2015; Li et al., 2020)
	Oct. 6–7 and 17–18, 2017	Jiageng	Modified from Jiang et al. (2008) + Picarro 2101i	This study
	Oct. 17, 2018	Jiageng	GO-8050 + Picarro 2301	This study
	Nov. 23–26, 2006	Dongfanghong 2	GO-8050 + Licor 7000	(Zhai et al., 2013; Li et al., 2020)
	Nov. 23–29, 2010	Dongfanghong 2	GO-8050 + Licor 7000	(Li et al., 2020)
	Nov. 27–28, 2022	Jiageng	GO-8050 + Picarro 2301	This study

later spring to summer. Among the freshwater inputs, the Han River mainly affects the water near the southern Taiwan Strait in summer (Li et al., 2000). Additionally, the study area is influenced by eastern Guangdong coastal upwelling in summer (Hu et al., 2003; Pan et al., 2011). Under the influence of the monsoon, the coastal current moves northeastward in summer and southwestward in winter (Hu et al, 2003). In winter, the freshwater discharge decreases, and under the influence of the northeasterly monsoon, the Zhejiang-Fujian Coastal Current (Zhe-Min Coastal Current, ZMCC) characterized by low temperature and low salinity flows into the study area. The Kuroshio Current also splits into a warm current through the Luzon Strait into the study area (Li et al., 2000), affecting the hydrological and biogeochemical characteristics of the study area.

Generally, the study area has high sea surface temperatures (SSTs) in summer and early fall but low SSTs in winter and early spring. In spring, the distribution of the isotherms and isohalines in the Taiwan Strait is generally parallel to the coastline, with sea surface salinities (SSSs) and SSTs gradually increasing from north to south, and increasing offshore. In summer, river inputs and coastal upwelling stimulate primary production on the shelf (Cao et al, 2011), but the slope is generally oligotrophic and characterized by low productivity (Chen, 2005).

For the convenience of calculation and discussion, we categorized the study area into three domains based on both topography and surface water pCO_2 distributions (Table S1). Domain I is the north of Taiwan Strait; domain II consists mainly the Taiwan Strait, and domain III is the area southwest of the Taiwan Shoal. We classify December-February as winter, March-May as spring, June-August as summer and September-November as fall following the studies in the East China Sea (Guo et al., 2015) and the South China Sea (Li et al., 2020).

2.2. Data collection

2.2.1. Measurements of surface water pCO_2 and auxiliary parameters

51 cruises were conducted in 2001–2022 in the southeastern coast of Mainland China onboard the R/Vs Jiageng (TKK), Dongfanghong 2, Yanping 2, Shiyan 3 and Kexue 3. Cruise periods and related information are listed in Table 1. During the cruises, SST, SSS and surface water pCO_2 were measured continuously. The measurement and data processing methods followed those of Pierrot et al. (2009) and were descripted in Li et al. (2020).

Surface water pCO_2 was measured continuously after air-sea CO_2 equilibration with a non-dispersive infrared spectrometer (Licor® 6252 or 7000) or a Cavity Ring-Down Spectroscopy (Picarro 2301 or 2101i) integrated in a GO-8050 system (General Oceanic Inc., USA) onboard Dongfanghong 2 and Jiageng, or with a homemade continuous measurement system onboard the other research vessels or Jiageng before June of 2018. Details of the information is provided in Table 1. The homemade system was described in Zhai et al. (2005; 2013). Surface seawater was continuously pumped from a depth of ~ 3–5 m into the air-sea equilibrator, where the seawater CO_2 reached equilibrium with the air CO_2 quickly. The equilibrated air was then extracted to the CO_2 detectors to measure CO_2 fraction (xCO_2) after removing the water vapor (Zhai et al., 2005; Dai et al., 2008; Guo et al., 2015). xCO_2 in the atmosphere was determined every ~ 1–1.5 h. The intake for atmospheric air samples was installed at the bow ~ 10 m above the sea surface to avoid contamination from the ships. CO_2 standards provided by National Research Center for Certified Reference Materials of China were used to calibrate the system every eight hours. The barometric pressure was measured continuously onboard with a barometer fixed ~ 10 m above the sea surface. Under field conditions, this method can achieve an analytical precision of ± 0.3% for xCO_2 (Zhai and Dai, 2009).

2.2.2. Wind speed, monthly average SST and SSS

Monthly average SST values were obtained from the National Oceanic and Atmospheric Administration (NOAA) of US high-resolution blended analysis of SST, version 2.1 (NOAA Physical Sciences Laboratory, Boulder, Colorado, USA, https://psl.noaa.gov). The optimum interpolation (OI) SST analysis is produced weekly on a 1° grid, and SST monthly fields are derived by a linear interpolation of the weekly fields to daily fields and then averaging the daily values over a month. The analysis uses in situ and satellite SST and SST simulated by sea-ice cover (Huang et al., 2021). Monthly average SSS values were obtained from NOAA, Global Ocean Data Assimilation System (GODAS, https://www.cpc.ncep.noaa.gov/products/GODAS/background.shtml). GODAS is a real-time ocean analysis and a reanalysis. The salinity data are provided at 0.333° spatial grid and it appears to reproduce observations quite well (Behringer and Xue, 2004). Daily wind speed data were acquired from the NASA, Jet Propulsion Laboratory Cross-Calibrated Multiple Platforms (CCMP) products with a spatial resolution of 0.25° (ftp://podaac-ftp.jpl.nasa.gov/allData/ccmp/L3.5a/).

The satellite-derived monthly average SST and SSS data are only used to get a big picture of the spatial and temporal variabilities of sea surface temperature and salinity of the study area. However, in all the calculations and discussions, the field measured data were adopted.

2.3. Data processing

2.3.1. pCO_2 calculations

Surface water pCO_2 at the temperature in the equilibrator (pCO_2^{Eq}) was calculated from xCO_2 of the dry air in the equilibrator and the pressure in the equilibrator (P_{Eq}) after correcting for the vapor pressure (P_{H2O}) of water at 100 % relative humidity (Weiss and Price, 1980) with Formula (1):

$$pCO_2^{Eq} = \left(P_{Eq} - P_{H_2O}\right) \times xCO_2 \quad (1)$$

Water pCO_2^{Eq} obtained from Formula (1) was corrected to pCO_2 at in situ temperatures (in situ pCO_2, or pCO_2 hereafter) using the empirical formula of Takahashi et al. (1993), where t is temperature in the equilibrator. The unit of both t and SST is °C.

$$in\ situ\ pCO_2 = pCO_2^{Eq} \times e^{(SST-t)\times 0.0423} \quad (2)$$

The surface water pCO_2 values at in situ temperature were normalized to 26 °C (long-term average temperature during the surveys) using Formula (3) (Takahashi et al., 2002). NpCO_2 values can eliminate the impact of temperature variability on surface water pCO_2, thereby better reflecting the influence of non-temperature processes on surface water pCO_2.

$$NpCO_2 = pCO_2 \times e^{(26-SST)\times 0.0423} \quad (3)$$

pCO_2 in the air was calculated using xCO_2 of atmosphere and the barometric pressure with a similar formula as Formula (1). Atmospheric xCO_2 from quasi-continuous measurements at Mauna Loa, Hawaii (19.5362°N, 155.5763°E, https://www.esrl.noaa.gov/gmd/dv/site/) was adopted to calculate the atmospheric pCO_2 after comparison with field measured values during the surveys as filed measured xCO_2 during some cruises were absent (Fig. S1).

2.3.2. Data normalization and gridding

Both the surface water and the atmospheric pCO_2 are increasing at global scale, and the rates differ in different regions for both surface water and the atmosphere (Kuttippurath et al., 2022; Roobaert et al., 2024). The surface water pCO_2 data used in this study were collected within two decades, so averaging them to the months and seasons would introduce bias, and time normalization is necessary. As there is no report on the surface water pCO_2 increasing rate, the same increasing rate as the atmospheric pCO_2 (2.0 μatm yr^{-1}) was used to normalize the surface water pCO_2 to the year 2010 following the studies in the East China Sea and the South China Sea (Guo et al., 2015; Li et al., 2020). However, the time-normalized pCO_2 data were only used to calculate the monthly and seasonal average pCO_2 values. For the air-sea CO_2 flux calculations,

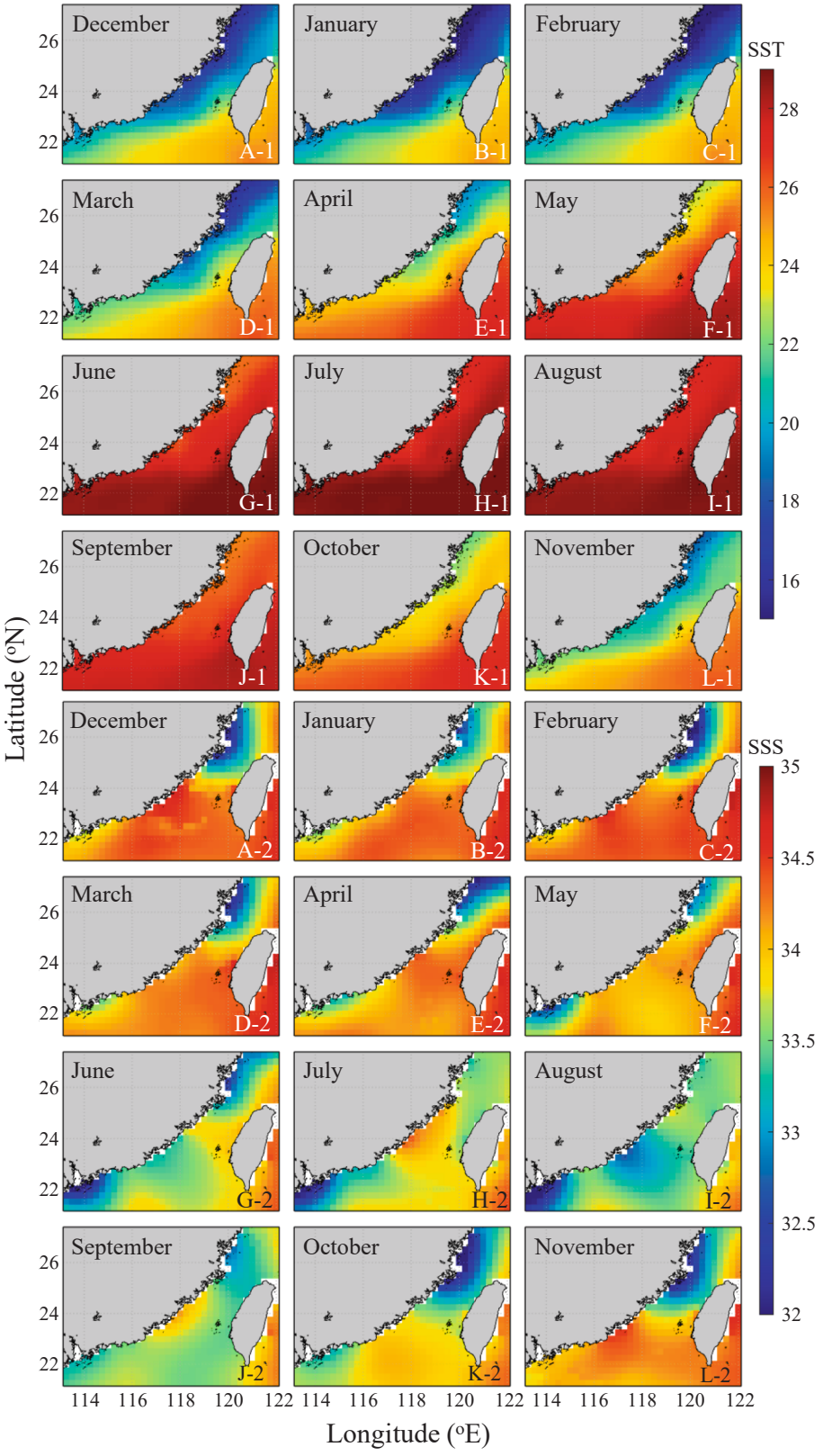

Fig. 2. Distributions of monthly average sea surface temperature (SST, in ℃) and sea surface salinity (SSS) in 2001–2022 in the southeastern coast of Mainland China. The monthly average SST values were obtained from the NASA ocean color website (http://oceancolor.gsfc.nasa.gov), which were retrieved from the Moderate Resolution Imaging Spectroradiometer (MODIS) onboard the Aqua satellite. The monthly average SSS values were obtained from NOAA, Global Ocean Data Assimilation System (GODAS) at http://www.cpc.ncep.noaa.gov/products/GODAS/background.shtml.

Table 2
Monthly and seasonal sea surface temperature, salinity, surface water pCO_2, atmospheric pCO_2 (Atm. pCO_2), pCO_2 difference between the surface water and the atmosphere (ΔpCO_2), wind speed, C_2 and air-sea CO_2 fluxes (FCO_2) in the three domains of the southeastern coast of Mainland China. October 2006 cruise was excluded in the calculations.

Season	Month	Domain	Temperature (℃)		Salinity		Water pCO_2 (μatm)		Atm. pCO_2 (μatm)		ΔpCO_2 (μatm)		Wind speed (m s^{-1})		C_2		FCO_2 (mmol m^{-2} d^{-1})	
			Average	SD	Average	SD	Average	SD	Average	SD	Average	SD	Average	SD	Average	SD	Average	SD
Winter	December	I	16.55	0.73	30.84	0.72	346.1	5.7	383.1	0.4	−37.0	5.3	10.49	0.47	1.06	0.01	−9.69	1.14
		II	17.04	0.58	31.34	0.73	356.2	14.3	382.9	0.3	−26.7	14.2	11.23	0.73	1.07	0.01	−8.19	4.99
		III	19.50	0.95	33.21	0.90	363.7	20.3	384.7	3.0	−21.0	18.1	11.50	0.82	1.04	0.01	−6.41	5.66
		Entire	17.78	1.47	31.87	1.27	356.6	16.7	383.5	2.0	−27.0	15.6	11.16	0.81	1.06	0.02	−7.90	4.87
	January	I	14.91	1.47	31.03	0.93	354.3	3.9	386.0	2.0	−31.7	4.3	9.93	0.67	1.09	0.02	−8.00	2.00
		II	15.47	1.90	31.28	1.24	351.4	6.6	386.7	1.5	−35.2	5.9	10.72	0.89	1.10	0.02	−10.08	2.37
		III	19.03	2.29	33.64	0.84	315.9	20.4	384.5	1.5	−68.6	20.4	10.38	0.85	1.07	0.01	−17.63	5.54
		Entire	16.69	2.70	32.12	1.58	338.7	22.2	385.7	1.9	−47.1	21.4	10.41	0.88	1.08	0.02	−12.47	5.61
	February	I	13.77	0.87	31.44	0.78	359.1	8.8	386.6	0.6	−27.4	8.3	8.78	0.08	1.16	0.01	−5.51	1.55
		II	14.11	0.97	31.57	0.56	358.1	14.5	388.3	2.8	−30.2	15.7	8.60	1.17	1.23	0.05	−6.58	4.12
		III	14.23	0.55	32.07	0.23	348.3	13.4	390.4	0.6	−42.1	13.3	8.50	1.20	1.16	0.05	−8.15	3.88
		Entire	14.06	0.89	31.67	0.62	355.9	14.1	388.4	2.5	–32.5	15.1	8.61	1.06	1.19	0.06	−6.73	3.81
	Seasonal		16.16	2.45	31.90	1.27	349.2	20.3	386.0	2.8	−36.7	19.9	10.05	1.38	1.11	0.07	−9.35	5.51
Spring	March	I	–	–	–	–	–	–	–	–	–	–	–	–	–	–	–	–
		II	17.50	2.04	32.91	0.85	342.6	23.6	386.3	1.4	−43.7	22.5	8.97	0.49	1.18	0.01	−9.44	5.40
		III	16.48	0.79	33.00	0.26	345.3	13.0	388.1	1.2	−42.8	11.9	7.61	0.85	1.15	0.01	−6.51	2.43
		Entire	17.02	1.67	32.95	0.65	343.8	19.5	387.2	1.6	−43.3	18.3	8.34	0.96	1.16	0.02	−8.08	4.52
	April	I	22.93	0.29	34.25	0.07	337.2	15.6	378.0	2.7	−40.8	15.6	7.64	0.09	1.12	0.01	−5.86	2.23
		II	22.53	1.99	34.13	0.31	352.3	15.0	380.6	3.4	−28.3	17.3	7.63	0.98	1.18	0.05	−4.39	3.33
		III	25.25	–	34.17	–	363.7	–	380.3	–	−16.6	–	7.93	–	1.32	–	−3.07	–
		Entire	22.70	1.81	34.16	0.27	349.5	16.3	380.1	3.4	−30.6	17.6	7.64	0.86	1.17	0.06	−4.65	3.15
	May	I	22.50	0.47	33.53	0.99	349.3	15.2	382.1	0.3	–32.7	15.3	6.67	0.21	1.21	0.01	−3.98	2.09
		II	23.70	1.08	33.95	0.62	371.7	21.1	381.3	1.9	−9.6	21.8	5.82	1.07	1.24	0.04	−1.06	2.39
		III	24.10	0.63	34.25	0.33	367.1	5.9	381.1	1.3	−14.0	6.4	5.48	0.45	1.24	0.03	−1.19	0.57
		Entire	23.59	1.05	33.95	0.69	366.8	19.5	381.4	1.6	−14.6	20.1	5.89	0.94	1.23	0.03	−1.59	2.32
	Seasonal		22.25	2.71	33.87	0.70	357.1	20.8	381.8	3.4	−24.7	21.8	6.89	1.36	1.20	0.05	−3.69	3.85
Summer	June	I	–	–	–	–	–	–	–	–	–	–	–	–	–	–	–	–
		II	25.99	0.83	33.36	0.67	401.9	20.2	378.7	1.5	23.2	19.0	4.93	0.65	1.19	0.04	1.31	1.36
		III	26.97	1.30	33.31	1.22	370.1	23.0	377.7	1.6	−7.6	22.1	5.72	0.49	1.15	0.02	−0.67	1.77
		Entire	26.49	1.20	33.33	0.99	385.6	26.9	378.2	1.6	7.4	25.7	5.33	0.70	1.17	0.04	0.29	1.87
	July	I	–	–	–	–	–	–	–	–	–	–	–	–	–	–	–	–
		II	27.27	1.62	32.88	0.71	393.0	33.0	374.3	2.3	18.7	31.6	5.00	0.55	1.20	0.05	0.95	1.71
		III	27.98	1.50	31.26	1.88	338.0	25.6	374.3	1.8	−36.4	25.3	5.19	0.55	1.20	0.03	−2.82	1.97
		Entire	27.69	1.59	31.91	1.72	360.0	39.4	374.3	2.0	−14.4	38.9	5.11	0.56	1.20	0.04	−1.31	2.63
	August	I	28.50	0.38	33.31	0.03	363.4	14.3	372.1	0.1	−8.7	14.3	7.09	0.09	1.43	0.06	−1.42	2.30
		II	27.88	1.22	33.22	0.34	377.9	36.6	372.4	1.3	5.5	36.2	5.37	1.05	1.33	0.08	−0.73	4.13
		III	28.74	1.05	32.82	0.24	361.3	34.0	371.5	1.4	−10.3	34.9	5.52	0.82	1.20	0.09	−0.48	2.08
		Entire	28.29	1.12	33.10	0.34	369.4	33.5	372.1	1.3	−2.7	33.5	5.76	1.08	1.31	0.12	−0.78	3.24
	Seasonal		27.59	1.50	32.80	1.27	371.1	35.2	374.5	3.0	−3.4	34.4	5.44	0.89	1.23	0.10	−0.64	2.79
Fall	September	I	26.30	0.11	33.11	0.29	402.8	8.7	374.7	0.2	28.2	8.9	9.16	0.39	1.12	0.02	6.05	2.35
		II	26.73	0.90	33.40	0.18	412.6	21.2	373.6	1.0	39.0	20.9	8.61	1.31	1.18	0.05	7.95	4.56
		III	28.52	1.45	33.37	0.29	368.4	4.5	371.8	0.9	−3.4	3.7	6.51	1.53	1.19	0.04	−0.29	0.24
		Entire	26.80	1.04	33.32	0.26	405.8	21.9	373.7	1.1	32.1	21.4	8.55	1.37	1.17	0.05	6.66	4.55
	October	I	–	–	–	–	–	–	–	–	–	–	–	–	–	–	–	–
		II	26.91	0.60	33.29	0.31	426.1	6.5	374.6	0.4	51.6	6.3	11.83	0.27	1.08	0.00	17.55	2.56
		III	28.06	0.96	33.68	0.12	387.7	14.3	373.6	0.9	14.1	14.7	10.88	0.73	1.09	0.02	4.54	4.36
		Entire	27.60	1.01	33.52	0.29	403.1	22.2	374.0	0.9	29.1	22.0	11.26	0.75	1.09	0.02	9.74	7.39
	November	I	21.53	1.72	32.74	1.14	370.2	7.9	379.1	1.7	−8.9	7.5	9.85	1.12	1.06	0.03	−2.04	2.21
		II	21.41	1.67	32.10	1.26	398.1	17.9	378.7	1.7	19.4	17.7	10.04	0.72	1.08	0.03	4.73	3.78
		III	22.96	1.52	33.34	0.74	357.4	20.9	377.8	1.3	−20.3	19.9	10.18	0.86	1.06	0.03	−5.38	5.05
		Entire	21.89	1.78	32.62	1.22	379.3	24.8	378.5	1.7	0.72	24.2	10.03	0.88	1.07	0.03	0.09	5.91
	Seasonal		24.42	2.98	33.00	0.97	391.8	26.7	376.2	2.8	15.6	27.6	9.74	1.41	1.11	0.06	3.80	6.98
Annual			22.72	4.98	32.84	1.30	366.8	31.2	379.5	5.6	−12.7	33.3	7.90	2.36	1.17	0.09	−2.63	6.81

–: No data.

pCO_2 data in the year of the surveys were adopted.

The surface water pCO_2 data at the year of the cruises, the time-normalized surface water pCO_2, the atmospheric pCO_2 and all auxiliary data were then averaged to 0.25° × 0.25° grids. Then monthly and seasonal averages were calculated to present the temporal variabilities.

2.3.3. Air-sea CO_2 flux calculation

Air-sea CO_2 fluxes (FCO_2) between the surface water and the atmosphere was calculated with Formula (4).

$$FCO_2 = k \times s \times \Delta pCO_2 = Tr \times \Delta pCO_2 \quad (4)$$

Where, k is gas transfer velocity and the empirical function of k with wind speed at 10 m above sea surface of Sweeney et al. (2007) was adopted; s is CO_2 solubility coefficient (Weiss, 1974); ΔpCO_2 is the pCO_2 difference between the surface water and the atmosphere; Tr is the air-sea gas transfer coefficient (Takahashi et al., 2009). For using monthly average wind speeds, nonlinear corrections (C_2) of gas transfer velocity were adopted following that of Wanninkhof et al. (2002) and Jiang et al. (2008). Therefore, k is calculated using Formula (5).

$$k = 0.27 \times C_2 \times U^2_{average} \times \left(\frac{Sc}{660}\right)^{-0.5} \quad (5)$$

In Formula (5), $U_{average}$ denotes the monthly average wind speed (in m s^{-1}); Sc denotes the Schmidt number at the in-situ temperatures for surface seawater (Wanninkhof, 1992).

C_2 denotes the nonlinear coefficient for the quadratic term of the gas transfer relationship, which was calculated using Formula (6).

$$C_2 = \left(\frac{1}{n}\sum_{i=1}^{n} U_i^2\right) \Big/ \left(U^2_{average}\right) \quad (6)$$

In Formula (6), U_i is the high-frequency (daily) wind speed and "n" is the number of available wind speed data in the month.

In this study, the average value for each parameter is presented as average ± standard deviation (SD).

2.3.4. Calculation of increasing rates of atmospheric and surface water pCO_2

It's worth to consider the interannual trends of atmospheric and surface water pCO_2 given that the data were collected over a 20-year

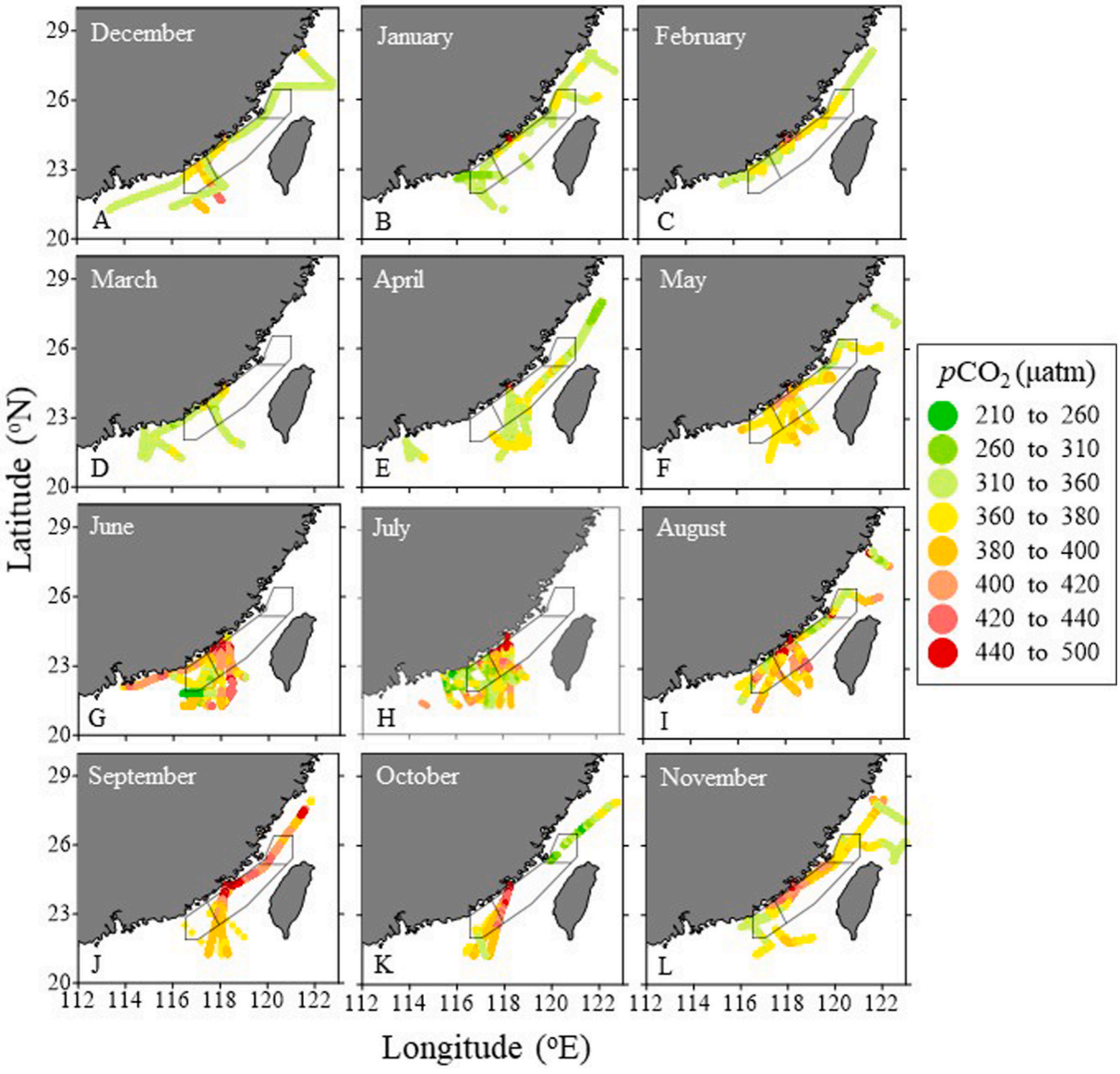

Fig. 3. Spatial distributions of surface water pCO_2 in the southeastern coast of Mainland China in the 12 months. Details of the cruises are in Tables 1-2. The surface water pCO_2 data were normalized to 2010. The circled areas are the three domains.

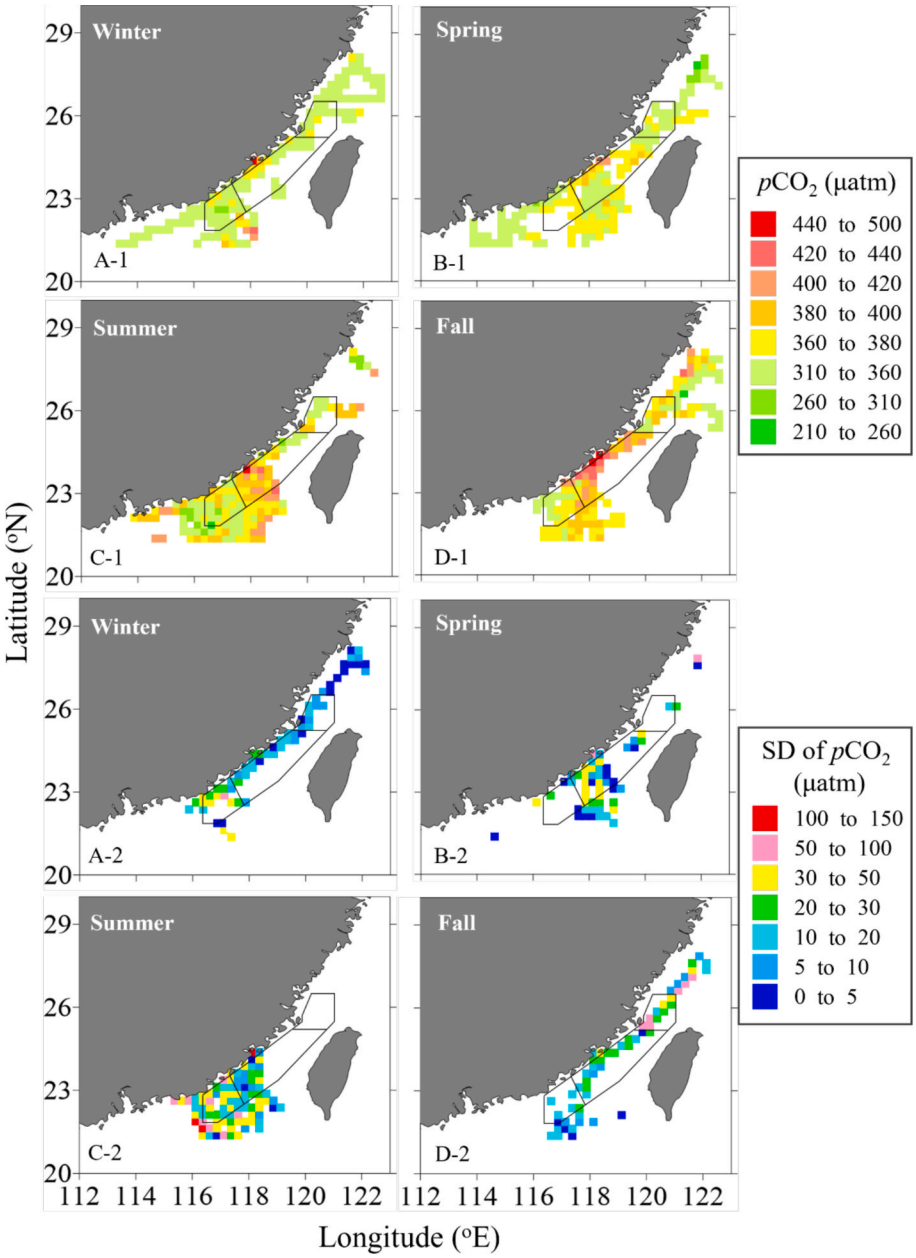

Fig. 4. Distributions of seasonal averages and standard deviations (SDs) of the surface water pCO_2 in the 0.25° × 0.25° grids in the southeastern coast of Mainland China. The surface water pCO_2 data were normalized to the year 2010. The circled areas are the three domains.

time span. Firstly, average pCO_2 of each cruise based on gridded data was calculated. Subsequently, the average pCO_2 data of each cruise was categorized by month to compute monthly and seasonal averages for each year; then annual averages were calculated. Finally, the increasing rates of atmospheric and surface water pCO_2 (and 95 % confidence intervals) were calculated using linear regression analysis with SPSS (version 19).

3. Results and discussions

3.1. SST and SSS

Seasonally, SST exhibited a seasonal pattern with the lowest temperatures in winter, gradually warming in spring, reaching highest SST in summer and early fall (Fig. 2). Spatially, SST gradually increased from north to south and increased offshore.

At monthly scale, the lowest SSTs occurred in January–February and the highest in July–August. Influence of the low-SST ZMCC was conspicuous in winter and early spring and retreated in May; its influence was conspicuous again from October (Fig. 2). In winter, SST ranged 14–25 ℃ and low-SST water occupied the entire study area. In spring, SST increased to 16–29 ℃ and it's much higher in May than in March. In spring, SSTs in March and April showed large spatial variability increasing southward. In summer, SST was highest but spatial and temporal variabilities were large. SSTs were relatively lower in June than in July and August. In July and August, relatively low SSTs (25.5–28.0 ℃) were in the near coast, and high SSTs (28.0–29.5 ℃) were in the southern zone of the study area. In fall, SSTs decreased and the relatively low-SST water occupied the entire study area from October. Seasonal variability amplitude of SST decreased gradually from north to south (Fig. 2). The seasonal variation of SST was due mainly to the influence of solar radiation and monsoon. SST were relatively low during the influence of the northeast monsoon in winter. In contrast, summer experienced higher SSTs as a result of the strong solar radiation

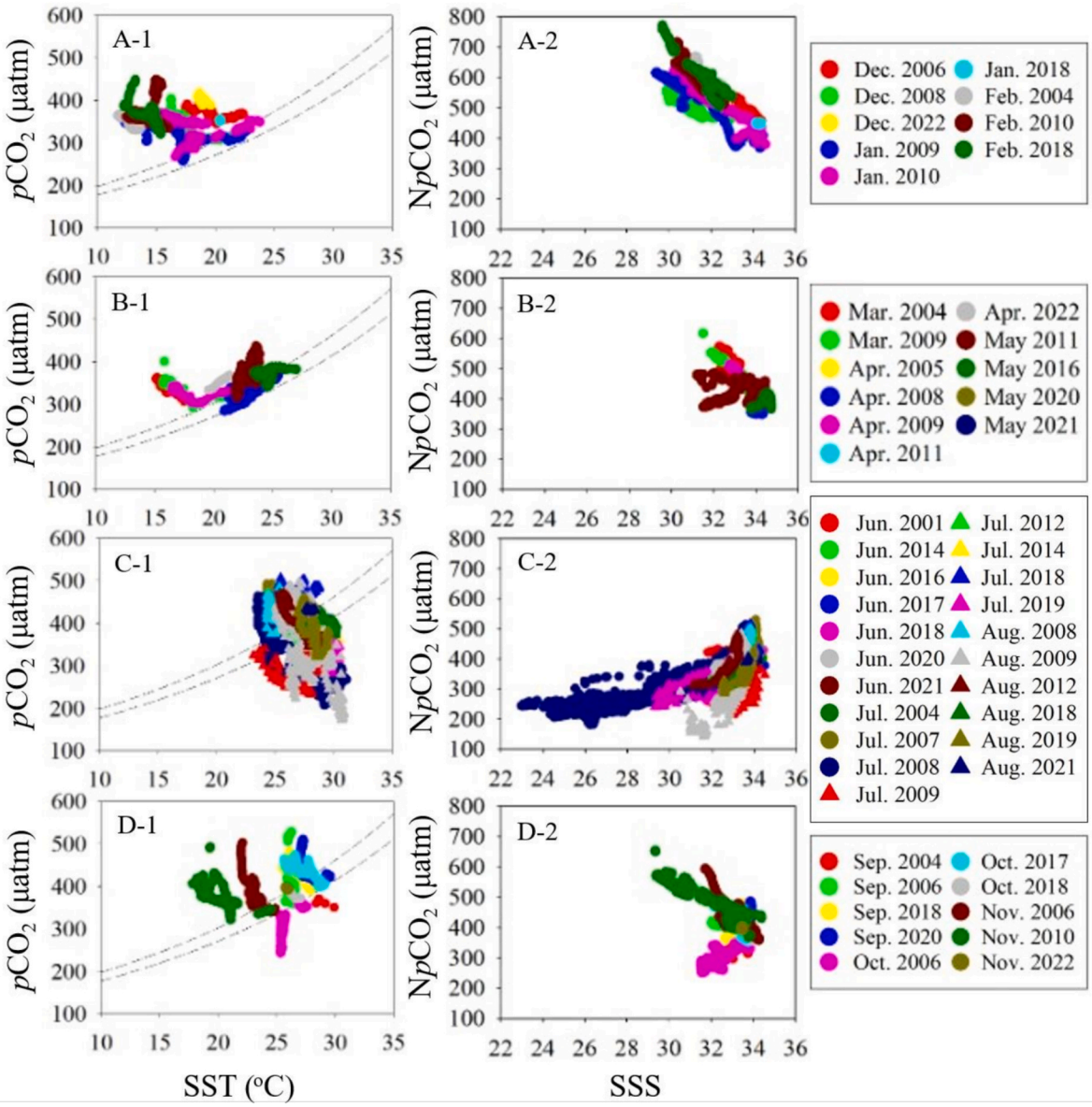

Fig. 5. Relationship of the surface water pCO_2 with sea surface temperature (SST), as well as normalized pCO_2 to 26°C ($NpCO_2$) with sea surface salinity (SSS). The dashed lines in panels A-1 to D-1 indicate the thermodynamically dominated pCO_2 range ($350 \times e^{(SST-26) \times 0.0423}$ and $390 \times e^{(SST-26) \times 0.0423}$) following Zhai et al. (2013).

and the effects of the subtropical high-pressure system under the influence of southeastern monsoon.

The distributions the field measured SSTs were consistent with those of the satellite monthly average SSTs. The seasonal average field measured SSTs were 16.16 ± 2.45 °C in winter, 22.25 ± 2.71 °C in spring, 27.59 ± 1.50 °C in summer, and 24.42 ± 2.98 °C in fall, respectively.

Different form the SST distribution, the spatial distribution of SSS was patchy and the spatial patterns of SSS differed among seasons. From December to April, and October to November, SSS was low in the northern zone and much higher in the southern zone (Fig. 2). From June to September, patches of the western coast exhibited typical characteristics of coastal upwelling, with distinct high salinities (Fig. 2 G-2 to J-2). Temporally, the low-SSS ZMCC was more pronounced from winter to mid spring (April) and again from October to November, while the influences of local river plumes were more conspicuous from May to August. Distributions of field measured SSS were consistent with those of the satellite monthly average SSSs. The seasonal average field measured SSSs were 31.90 ± 1.27 in winter, 33.87 ± 0.70 in spring, 32.80 ± 1.27 in summer, and 33.00 ± 0.97 in fall, respectively.

3.2. *Atmospheric pCO_2, wind speed and C_2*

Atmospheric xCO_2 showed an increasing trend from 370–373 μmol mol^{-1} in 2001 to 413–418 μmol mol^{-1} in 2022 with a seasonal amplitude of 5–7 μmol mol^{-1} at the Mauna Loa Observatory at Hawaii (Fig. S1). The cruise measured atmospheric xCO_2 was generally consistent with that of the Mauna Loa but with relatively larger seasonal variability, which might suggest stronger anthropogenic impacts in coastal zones (Fig. S1). The cruise average atmospheric pCO_2 ranged 317.8–390.4 μatm (Table 2).

Wind speed determines the air-sea gas transfer velocity. It may also influence the surface water pCO_2 through influencing vertical mixing of the water column. Generally, monthly average wind speeds over the entire study areas ranged from 5.11 to 11.26 m s^{-1} with annual average of 7.90 ± 2.36 m s^{-1} (Table 2). Wind speeds were high in fall (9.74 ±

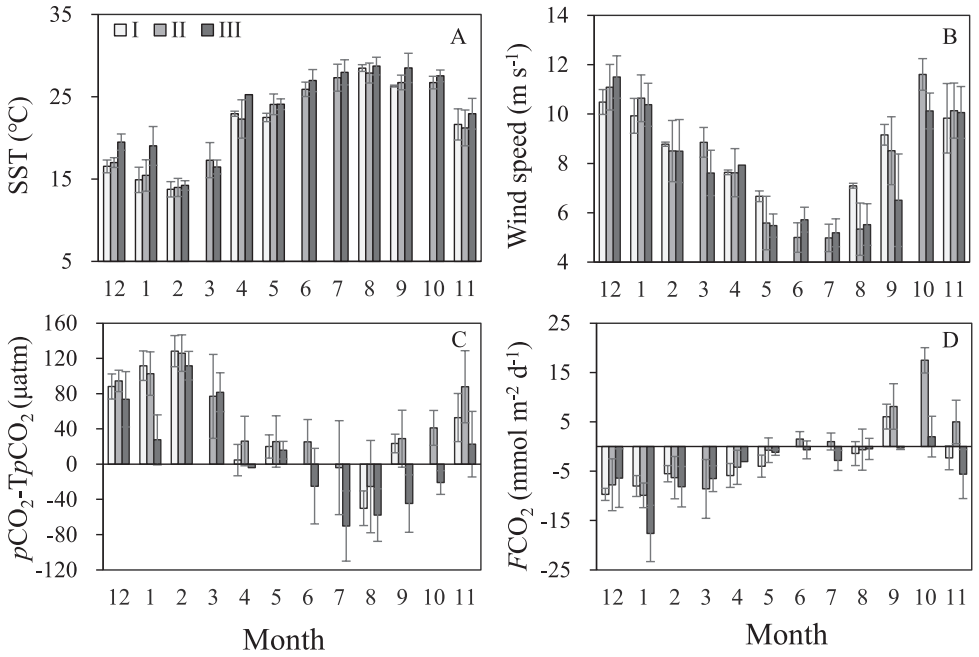

Fig. 6. Monthly sea surface temperature (SST), wind speed, difference of surface water pCO_2 and those at equilibrium with the atmosphere at in situ temperature (pCO_2-TpCO_2), and air-sea CO_2 fluxes (FCO_2) in the three domains (I, II and III) of the southeastern coast of Mainland China. The October 2006 cruise was excluded in the calculations.

1.41 m s^{-1}) and winter (10.05 ± 1.38 m s^{-1}), but low in spring (6.89 ± 1.36 m s^{-1}) and summer (5.44 ± 0.89 m s^{-1}), with inter-annual variations. The highest monthly average wind speeds were recorded in October and December (11.26 and 11.16 m s^{-1}), while the lowest wind speeds were in June and July (5.33 and 5.11 m s^{-1}, respectively). Due to the topography, wind speeds inside the Taiwan Strait were higher than those outside the strait.

C_2 values ranged from 1.06 to 1.31, with highest values in summer (1.23 ± 0.10), followed by spring (1.20 ± 0.05), and lowest in fall (1.11 ± 0.06) and winter (1.11 ± 0.07) (Table 2). The C_2 values in the study area were similar to those in the northern South China Sea (1.03–1.52, Li et al., 2020) and East China Sea (~ 1.20, Guo et al., 2015).

3.3. Surface water pCO_2 and its major controls

3.3.1. Spatiotemporal distributions of surface water pCO_2

Surface water pCO_2 showed conspicuous spatiotemporal variabilities (Fig. 3). The highest monthly average occurred in September, while the lowest monthly average was in January (Table 2). Surface water pCO_2 was generally low and horizontally homogenous in the cold months (300–360 µatm from December to April, Fig. 3A-E), except in the area near the Xiamen Bay and in the area west of the Luzon Strait in December of 2006 when winter upwelling occurred (Fig. 3A). However, in warm months from May to September, surface water pCO_2 exhibited large range from < 200 µatm to > 500 µatm (Fig. 3F-J). In May, surface water pCO_2 was relatively lower in the northern Taiwan Strait, and higher in the coastal zone of the southern Taiwan Strait (Fig. 3F). In summer (June-August), surface water pCO_2 in the study area was patchy, with high values in the Taiwan Shoal (>400 µatm), but low values (<360 µatm) in the area affected by the river plumes (Fig. 3G-I). In September and October, surface water pCO_2 in the Taiwan Strait was generally high (>400 µatm), except in the northern area in October of 2006 (Fig. 3K) when a fall bloom occurred (Guo et al., 2015). In November, surface water pCO_2 lowered to < 400 µatm in the offshore area although pCO_2 in the coastal zones was still > 400 µatm (Fig. 3L). Xiamen Bay and its surrounding waters maintained high surface water pCO_2 levels throughout the year (Fig. 3).

Surface water pCO_2 showed a clear seasonal pattern, with lower values in winter and spring, but higher values in summer and fall (Fig. 4). Seasonal average surface water pCO_2 were 349 ± 20, 357 ± 21, 371 ± 35 and 392 ± 27 µatm in winter, spring, summer and fall, respectively. In summer and fall, domain II showed higher average pCO_2 values than domains I and III (Fig. 4).

Standard deviations of seasonal surface water pCO_2 reflect the measurement errors, spatial variabilities, uncertainties induced by uneven sampling, etc, but mainly reflect the spatial and temporal variabilities. SDs of surface water pCO_2 ranged 20–35 µatm (Table 2). Relatively lower SDs occurred in winter (20 µatm) and spring (21 µatm), while relatively higher SDs were in summer (35 µatm), followed by fall (27 µatm) (Table 2 and Fig. 4). Very high SDs were in the southwestern zone of the study area in summer, where was influenced by the Pearl River plume water and eastern Guangdong coastal upwelling, and surface water pCO_2 showed large spatial and intra-seasonal variabilities.

3.3.2. Influencing factors of surface water pCO_2

The high variabilities of surface water pCO_2 suggest the impacts of complex regulating processes or factors. The influencing factors of surface seawater pCO_2 values include temperature effects, biological activities, water mixing, and the air-sea CO_2 exchange.

SST is an important factor influencing surface water pCO_2. $350 \times e^{(SST-26)\times 0.0423}$ and $390 \times e^{(SST-26)\times 0.0423}$ following Zhai et al. (2013) were adopted as the lower and upper limits of thermodynamically dominated pCO_2 (Fig. 5). In winter, pCO_2 was generally higher than the upper limit of the thermodynamically dominated pCO_2 range (Fig. 5A-1). NpCO_2 in winter was the highest among the four seasons, suggesting extra CO_2 added to the surface water, i.e. high-CO_2 bottom or subsurface water through vertical mixing. NpCO_2 decreased with salinity (Fig. 5A-2), suggesting water mixing between the high-NpCO_2 inshore water with the low-NpCO_2 offshore water.

In spring, most pCO_2 values were in the thermodynamically dominated pCO_2 range, with some data above the higher limit of the thermodynamically dominated pCO_2 range (Fig. 5B-1). The very high pCO_2 values were in early spring (March) in the inshore zones. NpCO_2 generally decreased with salinity, suggesting mixing of high-NpCO_2 inshore water with the relatively low-NpCO_2 offshore water (Fig. 5B-2). It is noteworthy that the data from the cruise in May 2011 exhibit two

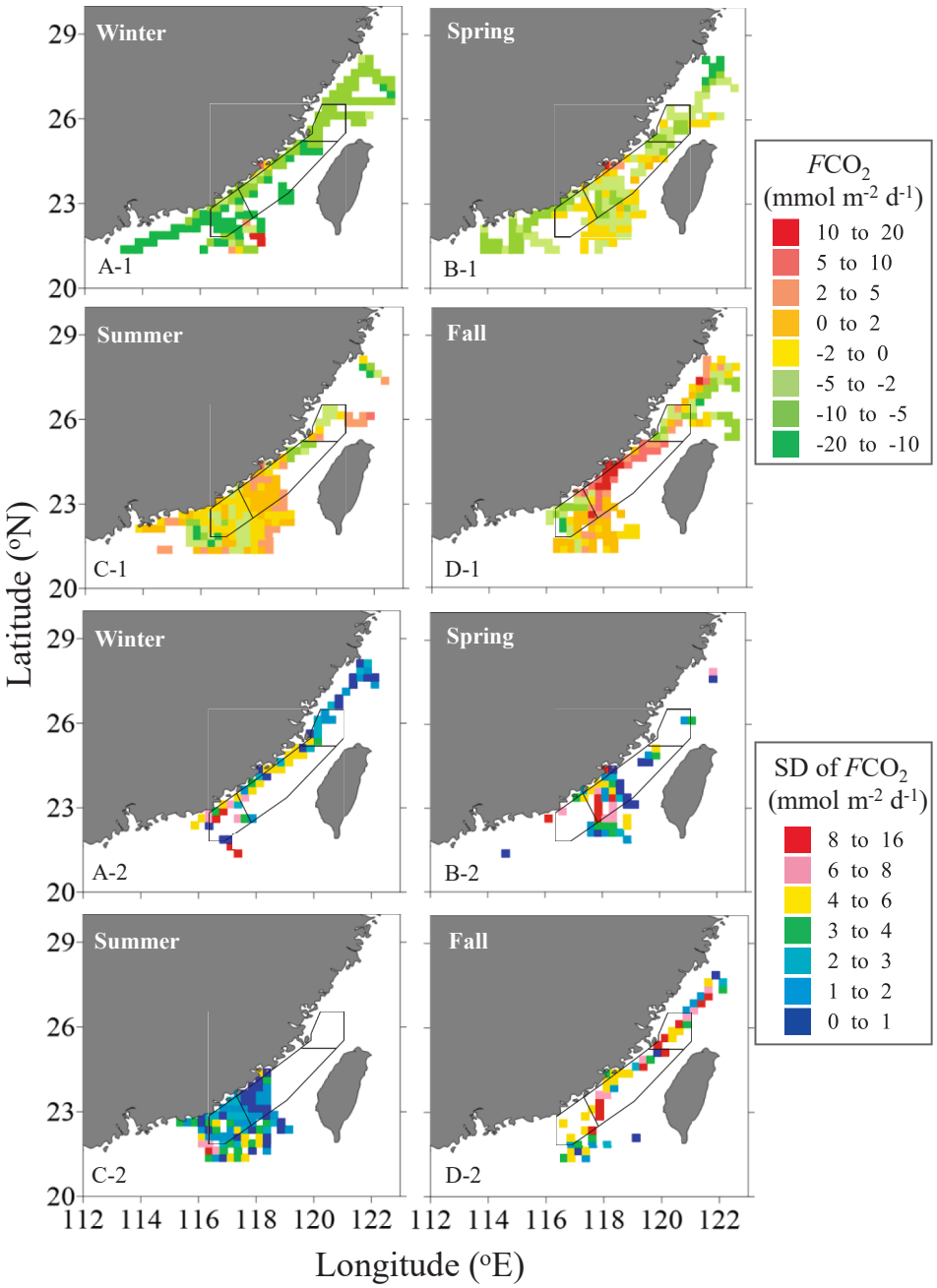

Fig. 7. Seasonal averages and standard deviations (SDs) of air-sea CO_2 fluxes (FCO_2) in the 0.25°× 0.25° grids in the southeastern coast of Mainland China. The circled areas are the three domains.

distinct branches: the low NpCO_2 data in domain I and the high NpCO_2 data in domain III (Fig. 5B-2).

In summer, most pCO_2 values were lower or higher than the thermodynamically dominated pCO_2 range, suggesting CO_2 removal or addition (Fig. 5C-1). The low pCO_2 values were in the river plumes and the high pCO_2 values were in the upwelling or the inshore zones. Generally, NpCO_2 increased with salinity during most summer cruises (Fig. 5C-2), indicating the water mixing among the plume water characterized by low salinity and low NpCO_2, the water in the upwelling characterized by high NpCO_2 and offshore surface water characterized by high salinity and medium NpCO_2. The very low NpCO_2 at the medium salinity during the July 2008 and 2009, August 2009 and June 2020 cruises were in the extended high-productive Pearl River plume characterized by strong biological CO_2 uptake (Cao et al., 2011; Yang et al., 2021).

During fall, most of the surface water pCO_2 values were higher than the higher limit of the thermodynamically dominated pCO_2 range except for the data collected at the north of the Taiwan Strait during October 2006 cruise when a phytoplankton bloom occurred (Fig. 3K; Fig. 5D-1). Relationship of NpCO_2 with salinity were generally similar with those in winter, except for the October 2006 cruise (Fig. 5D-2). During the October 2006 cruise, a fall bloom occurred, which was reported in Guo et al. (2015). In addition, the observations of high NpCO_2 at low salinities and low NpCO_2 at high salinities in winter, spring and summer suggest the mixing of high-NpCO_2 inshore surface water with the low-NpCO_2 offshore surface water.

Taking the SST-driven pCO_2 values at equilibrium with the atmosphere (TpCO_2) as a reference, the deviation of surface water pCO_2 from TpCO_2 (pCO_2-TpCO_2) represents the non-thermodynamically influenced pCO_2 (Zhai et al., 2025).

$$Tp\mathrm{CO_2} = p\mathrm{CO_{2,\,air}} \times e^{(\mathrm{SST}-26)\times 0.0423} \quad (7)$$

in which, $p\mathrm{CO_{2,air}}$ is the average atmospheric $p\mathrm{CO_2}$ during the cruise and 26°C is the long-term annual average SST.

$p\mathrm{CO_2}$-$Tp\mathrm{CO_2}$ shows a reverse monthly evolution pattern with that of SST (Fig. 6). In winter and early spring (March), $p\mathrm{CO_2}$-$Tp\mathrm{CO_2}$ was positive, suggesting CO_2 addition by vertical mixing of high-CO_2 subsurface water. From April, $p\mathrm{CO_2}$-$Tp\mathrm{CO_2}$ sharply reduced and became negative in July and August, indicating generally biological CO_2 uptake. In fall, $p\mathrm{CO_2}$-$Tp\mathrm{CO_2}$ became positive in the northern and central zones; and in November, $p\mathrm{CO_2}$-$Tp\mathrm{CO_2}$ became positive in the entire study area (Fig. 6G), suggesting net CO_2 addition to the surface water. The net addition of CO_2 resulting from vertical water mixing, combined with heating effect, ultimately led to the highest $p\mathrm{CO_2}$ values in fall.

To sum up, surface water $p\mathrm{CO_2}$ in the study area was primarily modulated by mixing and cooling during cold seasons, while upwelling and phytoplankton biological CO_2 uptake played significant roles during warm seasons.

There were four cruises in 2004 covering four seasons. Therefore, data of the 2004 cruises were taken as an example to determine the contribution of the factors controlling surface water $p\mathrm{CO_2}$ using a multiple linear regression (MLR) model. Detailed results are presented in Table S2. Firstly, the significance level of the analysis of variance was 0.000 (<0.05), indicating that the model is statistically significant. Secondly, the adjusted R^2 is 0.615, suggesting that the model can explain 61.5 % of the variability in surface water $p\mathrm{CO_2}$. The significance values for the SST, SSS, wind speed and atmospheric $p\mathrm{CO_2}$ were < 0.05, indicating that these factors all have significant effects on surface water $p\mathrm{CO_2}$, with SST being the primary influencing factor (Beta = 1.144), followed by atmospheric $p\mathrm{CO_2}$ (Beta = 0.613) and salinity (Beta = -0.680).

3.4. Air-sea CO_2 fluxes

3.4.1. Spatiotemporal distributions of air-sea CO_2 fluxes

Air-sea CO_2 fluxes also showed conspicuous seasonal and spatial variabilities. In winter, the study area was generally a moderate to a strong CO_2 sink and the air-sea CO_2 fluxes was relatively homogeneous, with air-sea CO_2 flux values of –32.0 to 0.8 mmol m^{-2} d^{-1}. The exception was the southwestern zone of the study area in December 2006 when a winter upwelling was observed (Zhai et al., 2013) (Fig. 7A-1). In spring, the values of air-sea CO_2 fluxes (−18.4 to 2.8 mmol m^{-2} d^{-1}) were generally higher than in winter, and the southern zone of the study area and the middle Taiwan Strait became near equilibrium with the atmosphere or even a CO_2 source (Fig. 7B-1). In summer, most of domain II became a weak CO_2 source, while domain I was generally still a CO_2 sink except southwestern area of domain I, where was influenced by upwelling, acting as a weak CO_2 source. The limited area influenced by river plumes in domain III also acted as a weak CO_2 sink in summer (Fig. 7C-1). The air-sea CO_2 fluxes of the whole study area in summer ranged from −9.6 to 5.3 mmol m^{-2} d^{-1}. In fall, spatial variation of the air-sea CO_2 fluxes was very large (Fig. 7D-1). In November, domain II was a moderate to strong CO_2 source, while domains I and III acted as a moderate CO_2 sinks (Fig. 6D). The air-sea CO_2 fluxes in fall ranged −10.9 to 21.4 mmol m^{-2} d^{-1}.

Spatially, annual average air-sea CO_2 fluxes showed distinct regional characteristics (Fig. S2). Domains I and III acted as CO_2 sinks with annual average air-sea CO_2 fluxes of −4.4 ± 2.6 and −4.2 ± 4.5 mmol m^{-2} d^{-1}, respectively. The strong CO_2 sink in domain I in winter and the river plume in domain III in summer contributed much to the annual CO_2 sink. The coastal zone of the southern domain II (from Xiamen Bay to the coast off Shantou) acted as CO_2 source of 5–15 mmol m^{-2} d^{-1}. This was due mainly to the high surface water $p\mathrm{CO_2}$ off the Xiamen Bay in all seasons and the high $p\mathrm{CO_2}$ in coastal upwelling in summer in the coast off Shantou (Fig. 4). Domain II as a whole was generally near equilibrium with the atmosphere with annual average air-sea CO_2 flux of −0.4 ± 7.9 mmol m^{-2} d^{-1}.

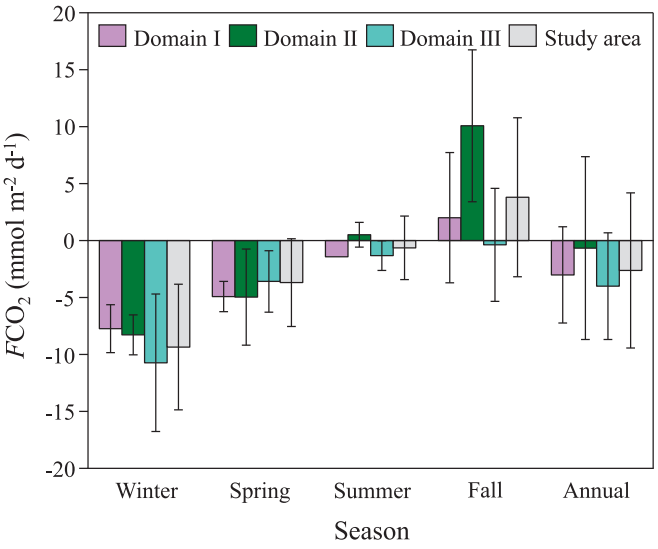

Fig. 8. Seasonal and annual average air-sea CO_2 fluxes in the southeastern coast of China. The gray columns are seasonal averages.

The intra-seasonal variation in the air-sea CO_2 fluxes was generally low in winter (< 1-fold variations) and spring (1- to 2-fold variations), higher in summer (2- to 7-fold) and reaching the peak in fall (more than 20-fold). In early fall (September), surface water $p\mathrm{CO_2}$ was highest throughout the year, and the rapidly decreased SST in late fall (November, 5.7°C lower than in October) caused the study area turned from a strong CO_2 source to near equilibrium with the atmosphere, resulting in very large intra-seasonal variation (Fig. 8).

The study area as a whole is a CO_2 sink of 9.4 ± 5.5 and 3.7 ± 3.9 mmol m^{-2} d^{-1} in winter and spring, respectively, and a CO_2 source of 3.8 ± 7.0 mmol m^{-2} d^{-1} in fall. In summer, it is near equilibrium with the atmosphere with an air-sea CO_2 flux of −0.6 ± 2.8 mmol m^{-2} d^{-1}. Annually, the study area acts as a weak to moderate sink of 2.6 ± 6.8 mmol m^{-2} d^{-1}.

The surface water $p\mathrm{CO_2}$ showed an increase rate of 1.88 ± 20.86 μatm yr^{-1} (n = 18, R^2 = 0.26, p < 0.05, Fig. 9A), which was similar to that of the atmospheric $p\mathrm{CO_2}$ of 1.93 ± 3.37 μatm yr^{-1} (n = 18, R^2 = 0.93, p < 0.0001, Fig. 9B). The growth rates of surface water $p\mathrm{CO_2}$ and atmospheric $p\mathrm{CO_2}$ were analyzed using an interaction term regression model. The calculated p value is 0.9568 (>0.05), suggesting that their growth rates have no significant difference. As a result, $F\mathrm{CO_2}$ did not exhibit a conspicuous long-term trend under the influence of the large inter-annual variability (Fig. 9C).

3.4.2. Regulating factors of air-sea CO_2 fluxes

The calculated air-sea CO_2 fluxes in this study are dominated by$\Delta p\mathrm{CO_2}$, CO_2 solubility coefficient (s) and gas transfer velocity (k), the latter of which is calculated with wind speed (Formulae 4 and 5).

$\Delta p\mathrm{CO_2}$ determines the direction of the air-sea CO_2 exchanges. The study area is a CO_2 sink of 9.4 ± 5.5 and 3.7 ± 3.9 mmol m^{-2} d^{-1} in winter and spring, the negative $\Delta p\mathrm{CO_2}$ (−36.7 ± 19.9 and −24.7 ± 21.8 μatm) played a crucial role. Despite the fact that the vertical mixing during cold seasons contributes to an increase in surface water $p\mathrm{CO_2}$ by 50–200 μatm (Fig. S3 A-1), the cooling effect decreased $p\mathrm{CO_2}$ by 200–300 μatm (Fig. S3 A-2), resulting in more negative $\Delta p\mathrm{CO_2}$, In summer, the very weak air-sea CO_2 flux was dominated by the very close surface water $p\mathrm{CO_2}$ with the atmospheric $p\mathrm{CO_2}$ (Table 2). The increase in surface water $p\mathrm{CO_2}$ caused by upwelling partially offset the $p\mathrm{CO_2}$ decrease by biological CO_2 removal (Fig. S3 C-1), combined with heating effect (Fig. S3 C-2), ultimately leads to a nearly equilibrium of surface water $p\mathrm{CO_2}$ with the atmosphere. In fall, the CO_2 source of 3.8 ± 7.0

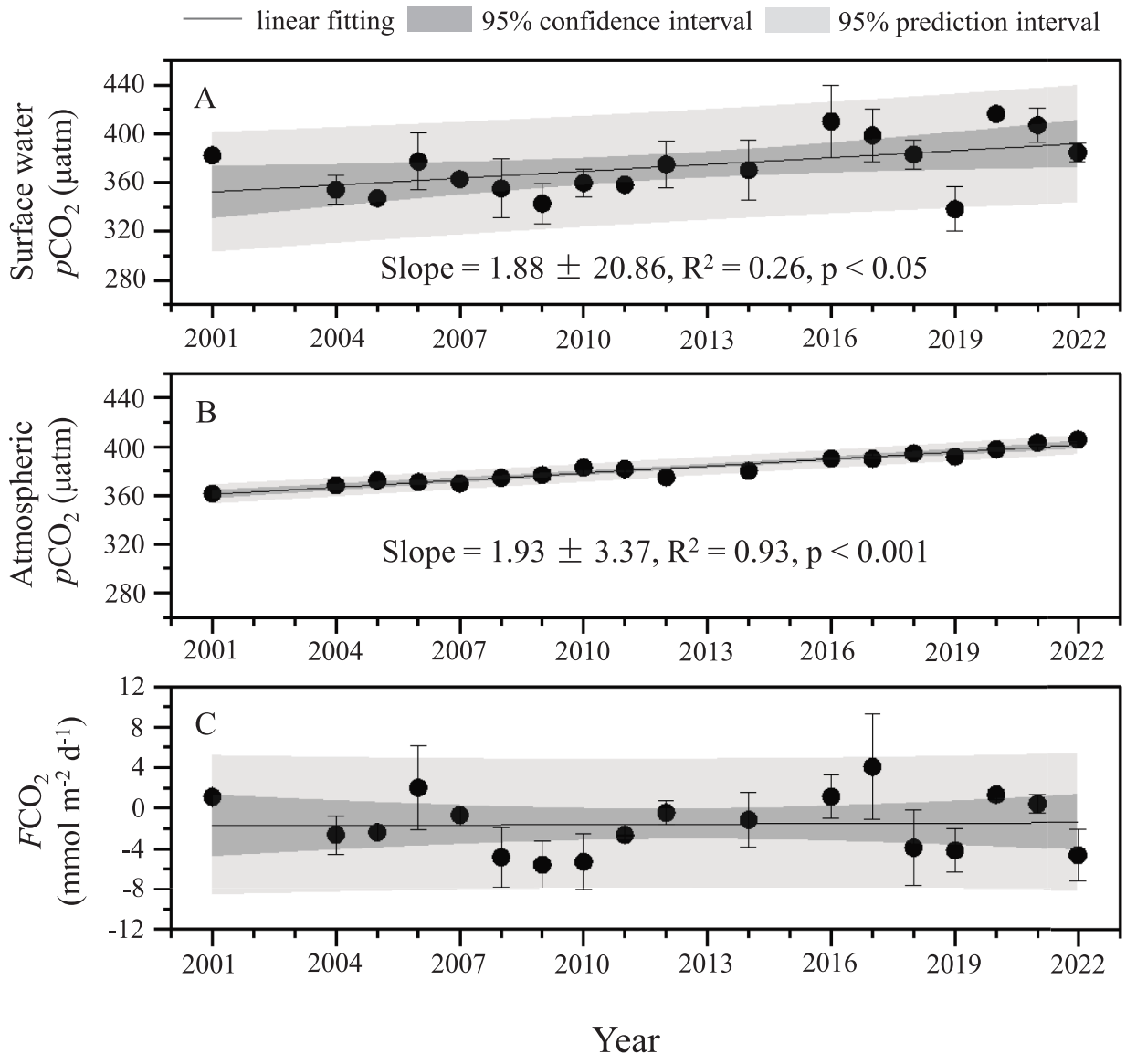

Fig. 9. Multi-year trends of sea surface pCO_2, atmospheric pCO_2 and air-sea CO_2 fluxes (FCO_2) in the southeastern coast of Mainland China.

mmol m^{-2} d^{-1} was dominated by the positive ΔpCO_2 (15.6 ± 27.6 μatm), which is due mainly to the destruction of the stratification (Fig. S3 D-1) and mixing of high-pCO_2 subsurface water but weak cooling effect (Fig. S3 D-2, Zhai and Dai, 2009). Both thermal and non-thermal pCO_2 changes in the southeastern coast of Mainland China are much stronger than the coastal northern Indian Ocean (Peter et al., 2025), which might be due to the fact that our study area is more nearshore than those of Peter et al. (2025).

The calculated gas transfer coefficient ($Tr = k \times s$) is determined by wind speed, SST and SSS (Formulae 4 and 5). In this study, field measured SSTs and SSSs combined with monthly average wind speeds from remote sensing were used to calculate the gas transfer coefficients. The *Tr* trend was basically consistent with that of wind speed, and had less influence by SSS (Fig. 10). In fall and winter, higher wind speeds led to higher gas transfer coefficients, which to some extent enhanced CO_2 release or absorption. Additionally, wind speed is a critical variable determining the mixed layer depth of the sea (Large et al., 1994), and higher wind speeds may cause a rise in surface water pCO_2 due to enhanced vertical mixing as well as other associated changes in marine biogeochemistry (Takahashi et al., 2009).

To further quantify the impact of ΔpCO_2, wind speed and temperature on the air-sea CO_2 fluxes, a control variable method was employed for the analysis. Under the assumption that changes in temperature equivalently alter atmospheric and surface water pCO_2 without affecting ΔpCO_2, the deviations of SST and wind speed from the annual average for each season were calculated, which is allowed to determine the resulting shifts in air-sea CO_2 fluxes. The amount of change could be obtained as follows:

$$\Delta X = X_{\text{seasonal}} - X_{\text{annual}} \tag{8}$$

$$\Delta FCO_2 = FCO_{2,\ \text{seasonal}} - FCO_{2,\ \text{annual}} \tag{9}$$

Where X_{seasonal} and X_{annual} is seasonal and annual average value of the parameters, respectively; Δ is the change; $FCO_{2,\text{annual}}$ is the annual average air-sea CO_2 fluxes, calculated using the annual average values of other parameters. By varying one parameter, the corresponding FCO_2 change (ΔFCO_2) can be derived.

Table 3 illustrates the effects of seasonal variations in ΔpCO_2, wind speed and SST on FCO_2 and *Tr*. ΔpCO_2 was the primary drivers of changes in FCO_2, and it exhibited the largest impact in fall and winter (changes in FCO_2 by 189.0 % and 222.8 %, respectively). In contrast,

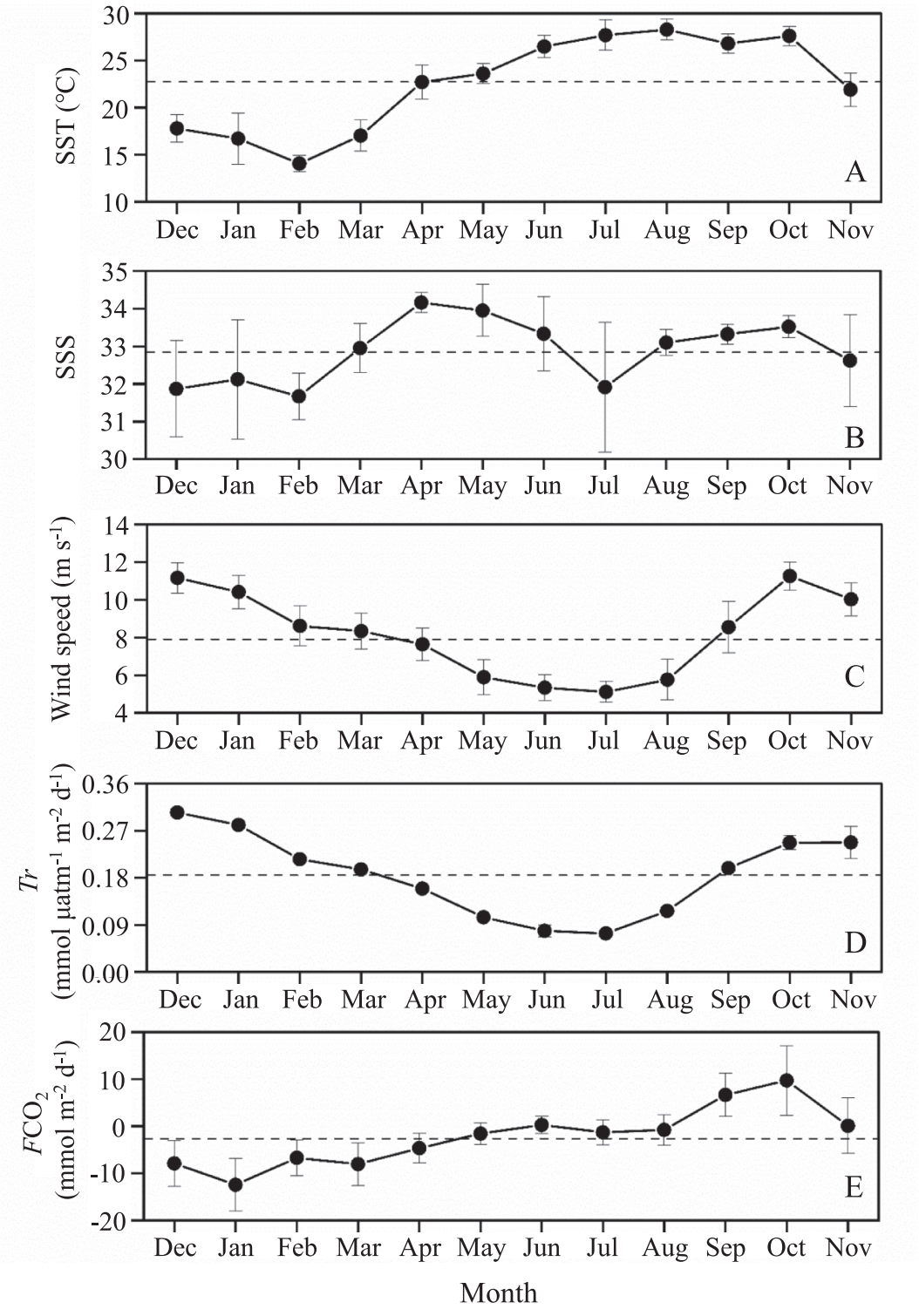

Fig. 10. Monthly variations of sea surface temperature (SST), salinity (SSS), wind speed, *Tr*, and air-sea CO_2 fluxes (FCO_2) in the southeastern coast of Mainland China. The dashed lines are annual averages; error bars are standard deviations.

ΔpCO_2 showed a relatively smaller effect in spring and summer, contributing to changes in FCO_2 by 94.5 % and 73.2 %, respectively. Variations in wind speed also had a substantial impact on *Tr*, ultimately enhancing CO_2 absorption or release notably. During winter, high wind speed increased CO_2 sink to 3.39 mmol m^{-2} d^{-1}, representing a 61.8 % enhancement compared to the annual average of 2.10 mmol m^{-2} d^{-1}. Variations in wind speed had the similar relative impact on FCO_2 in summer and fall (52.6 % and 52.0 %, respectively), and exhibited the smallest effect (23.9 %) in spring. Compared with ΔpCO_2 and wind speed, the contribution of SST change (through influencing CO_2 solubility) to FCO_2 changes was minor. In winter, SST contributed to a 2.2 % reduction in FCO_2 through its effect on *Tr* (2.1%), and its effect to the changes in *Tr* and FCO_2 during the other three seasons were negligible (less than 0.5 %).

Seasonally, FCO_2 was largely affected by these factors in winter (377.8 %), followed by fall (286 %), summer (87 %), and least in spring

Table 3
Changes and percentage variations in *Tr* and air-sea CO_2 fluxes (FCO_2) affected by the seasonal variations of ΔpCO_2, SST and wind speed.

Season	Variates	ΔTr (mmol μatm^{-1} m^{-2} d^{-1})	ΔFCO_2 (mmol m^{-2} d^{-1})
Winter	ΔpCO_2	–	−3.9637 (189.0 %)
	SST	0.0035 (2.1 %)	−0.0454 (2.2 %)
	Wind speed	0.1021 (61.8 %)	−1.2970 (61.8 %)
	Seasonal	0.1079 (65.3 %)	−7.9242 (377.8 %)
Spring	ΔpCO_2	–	−1.9818 (94.5 %)
	SST	0.0002 (0.1 %)	−0.0027 (0.1 %)
	Wind speed	−0.0396 (24.0 %)	0.5021 (23.9 %)
	Seasonal	−0.0394 (23.8 %)	−1.0095 (48.1 %)
Summer	ΔpCO_2	–	1.5360 (73.2 %)
	SST	−0.0007 (0.4 %)	0.0086 (0.4 %)
	Wind speed	−0.0869 (52.6 %)	1.1029 (52.6 %)
	Seasonal	−0.0872 (52.8 %)	1.8323 (87.4 %)
Fall	ΔpCO_2	–	4.6739 (222.8 %)
	SST	−0.0007 (0.4 %)	0.0081 (0.4 %)
	Wind speed	0.0858 (51.9 %)	−1.0908 (52.0 %)
	Seasonal	0.0849 (51.4 %)	5.9987 (286.0 %)

–: No data.

Table 4
Comparison of the annual average air-sea CO_2 fluxes of the southeastern coast with the East China Sea and the northern South China Sea (unit: mmol m^{-2} d^{-1}).

Study area	Winter	Spring	Summer	Fall	Annual	Data source
Southeastern coast of Mainland China	−9.4 ± 5.5	−3.7 ± 3.9	−0.6 ± 2.8	3.8 ± 7.0	−2.6 ± 6.8	This study
Coastal zone of the East China Sea	−8.9 ± 1.4	−10.7 ± 3.5	−2.4 ± 3.3	0.7 ± 4.1	−5.3 ± 3.7	Guo et al. (2015)
Northern South China Sea shelf	−7.4 ± 3.9	−2.8 ± 2.5	−0.2 ± 4.4	1.2 ± 2.8	−2.3 ± 3.5	Li et al. (2020)

(48 %). This seasonal disparity might stem from the fact that spring was closest to the annual averages. Additionally, during winter and summer, the synergistic effects of the three parameters enhanced CO_2 absorption or release, whereas wind speed acted antagonistically with SST and ΔpCO_2 in spring and fall. Overall, the estimates demonstrate that winter was the season in which various parameters exerted the greatest influence on FCO_2, and higher wind speed significantly increased *Tr*, ultimately enhancing CO_2 absorption. Detailed data are shown in Table S3.

MLR analysis was employed to verify the above results. Detailed results are presented in Table S4. The results indicated that SST, ΔpCO_2 and wind speed significantly influence the changes of FCO_2, while salinity had no significant effect ($p > 0.05$). Among these factors, ΔpCO_2 was identified as the primary determinant of FCO_2 variation (Beta = 0.744), followed by wind speed (Beta = -0.472), while SST (through influencing CO_2 solubility) has a relatively minor impact (Beta = -0.179). The statistic results support the results drawn from the control variable method adopted in the above calculations.

3.4.3. Comparing air-sea CO_2 fluxes with the adjacent shelf seas

We obtained an overview of the seasonal and spatial variation in air-sea CO_2 fluxes in the southeastern coast of Mainland China (Table 2). The study area as a whole, the CO_2 sink in the study area in winter (9.4 ± 5.5 mmol m^{-2} d^{-1}) is similar to that of the East China Sea (ECS) coast (8.9 ± 1.4 mmol m^{-2} d^{-1}), but slightly stronger than the northern South China Sea (NSCS) shelf (7.4 ± 3.9 mmol m^{-2} d^{-1}). In spring, the CO_2 sink in the study area (3.7 ± 3.9 mmol m^{-2} d^{-1}) is similar to or slightly stronger than the NSCS shelf (2.8 ± 2.5 mmol m^{-2} d^{-1}), but much weaker than the ECS coast (10.7 ± 3.5 mmol m^{-2} d^{-1}). In summer, CO_2 in the study area is close equilibrium with the atmosphere, which is similar to the case of the NSCS shelf, but the ECS coast is a CO_2 sink of 2.4 ± 3.3 mmol m^{-2} d^{-1}. In fall, the CO_2 source in the study area (3.8 ± 7.0 mmol m^{-2} d^{-1}) is stronger than both the ECS coast (0.7 ± 4.1 mmol m^{-2} d^{-1}) and the NSCS shelf (1.2 ± 2.8 mmol m^{-2} d^{-1}). Annually, the CO_2 sink in the study area (2.6 ± 6.8 mmol m^{-2} d^{-1}) is the same as that of previous study conducted in this area (2.58 mmol m^{-2} d^{-1}; Chen, 2009), and similar to that of the NSCS shelf (2.3 ± 3.5 mmol m^{-2} d^{-1}), but much weaker than that of the ECS coast (5.3 ± 3.7 mmol m^{-2} d^{-1}) (Table 4).

In the ECS coast, the low SST in winter, the strong biological CO_2 uptake in spring and summer stimulated by the Changjiang nutrient input leads to the strong CO_2 sink (Guo et al., 2015). The weaker CO_2 sink of the study area than the East China Sea might be due mainly to the coastal upwelling in summer, higher temperature, and the weaker biological CO_2 uptake in warm seasons. It is more resemble to the NSCS shelf.

3.5. Uncertainty and limitation

As can be seen in Fig. S2, there are still several grids without data in domain II, which may bring bias to the air-sea CO_2 flux estimation. A statistical analysis using SPSS (version 19) involving 1000 bootstrap resampling on the grid data from domain II was conducted, comprising 92 grids. The results indicated that the 95 % confidence interval for the average of the key metrics ranged from 411 to 434 μatm, suggesting a narrow interval, which demonstrates that the estimates based on the current dataset exhibit good stability. This implies that the results for the measured regions in domain II are likely to represent the entire domain II effectively.

In addition to the spatial coverage, the unevenly seasonal coverage is also a potential source of uncertainty. The dataset spans a considerable time frame, with 51 cruises unevenly distributed across the four seasons. The seasonal and annual average values may be subject to errors due to seasonal variations and insufficient temporal coverage. There are also differences in surface water pCO_2 among the three domains. Not all the cruises cover all the three domains, which may limit the accuracy of the estimated air-sea CO_2 fluxes.

Additionally, the cruises were conducted in relatively good sea state, and the direct influence of severe sea condition, such as typhoons or tropical storms, is not included in the estimates of this study. The influence of typhoon on the surface water pCO_2 and air-sea CO_2 fluxes in China Seas are under study combing the field observational data, data construction, remote sensing and model results.

4. Concluding remarks

Surface water pCO_2 and air-sea CO_2 fluxes in the southeastern coast of Mainland China showed significant spatiotemporal variations. Surface water pCO_2 was lowest in winter (349 ± 20 μatm), increased to 357 ± 21 μatm in spring, 371 ± 35 μatm in summer and 392 ± 27 μatm in fall. The study area acted as a moderate to strong CO_2 sink of 9.4 ± 5.5 and 3.7 ± 3.9 mmol m^{-2} d^{-1} in winter and spring, near equilibrium with the atmosphere in summer and a moderate source of 3.8 ± 7.0 mmol m^{-2} d^{-1} in fall. Annually, the study area is a CO_2 sink of 2.6 ± 6.8 mmol m^{-2} d^{-1}, similar to the northern South China Sea shelf, but much weaker than the East China Sea coast. Seasonal variation of ΔpCO_2 and wind speed played important roles in the seasonal variation in air-sea CO_2 fluxes. Cooling is the primary controlling factors of the low surface water pCO_2 and negative ΔpCO_2 during the cold seasons. In contrast, vertical mixing and heating is the major reason of the high surface water pCO_2 and positive ΔpCO_2 in fall.

CRediT authorship contribution statement

Dezhi Bu: Conceptualization, Data curation, Methodology, Visualization, Writing – original draft, Writing – review & editing. **Xianghui Guo:** Conceptualization, Data curation, Funding acquisition,

Investigation, Methodology, Writing – original draft, Writing – review & editing. **Weidong Zhai:** Conceptualization, Data curation, Investigation, Visualization, Writing – review & editing. **Yi Xu:** Data curation, Investigation, Methodology, Writing – review & editing. **Minhan Dai:** Funding acquisition, Investigation, Project administration, Writing – review & editing.

Declaration of competing interest

The authors declare that they have no known competing financial interests or personal relationships that could have appeared to influence the work reported in this paper.

Acknowledgements

The crews, scientific staffs and chief scientists of the R/Vs Jiageng, Yanping 2, Dongfanghong 2, Shiyan 3, Kexue 3 were appreciated for their help during the cruises. Xirong Chen, Yizheng Xu, Baoshan Chen, Yuancheng Su, Gui Chen, Yan Li, Jinwen Liu and Yi Wang are appreciated for collecting data during some cruises. The study was supported by the Natural Science Foundation of China (42141001 and 42188102).

Appendix A. Supplementary data

Supplementary data to this article can be found online at https://doi.org/10.1016/j.pocean.2025.103659.

Data availability

Data will be made available on request.

References

Behringer, D.W., Xue, Y., 2004. Evaluation of the global ocean data assimilation system at NCEP: the Pacific Ocean. Eighth Symposium on Integrated observing and Assimilation Systems for Atmosphere, Oceans. In: And Land Surface, AMS 84th Annual Meeting. Washington State Convention and Trade Center, Seattle, Washington, pp. 11–15.

Borges, A.V., Frankignoulle, M., 1999. Daily and seasonal variations of the partial pressure of CO_2 in surface seawater along Belgian and southern dutch coastal areas. J. Mar. Syst. 19, 251–266.

Borges, A.V., Delille, B., Frankignoulle, M., 2005. Budgeting sinks and sources of CO_2 in the coastal ocean: Diversity of ecosystems counts. Geophysical Research Letter 32, L14601.

Cai, W.-J., 2011. Estuarine and coastal ocean carbon paradox: CO_2 sinks or sites of terrestrial carbon incineration? Ann. Rev. Mar. Sci. 3, 123–145.

Cai, W.-J., Dai, M., Wang, Y., 2006. Air-sea exchange of carbon dioxide in ocean margins: a province-based synthesis. Geophys. Res. Lett. 33, 347–366.

Cao, Z., Dai, M., Zheng, N., Wang, D., Li, Q., Zhai, W., Meng, F., Gan, J., 2011. Dynamics of the carbonate system in a large continental shelf system under the influence of both a river plume and coastal upwelling. J. Geophys. Res. Biogeo. 116, G02010.

Chen, Y.L.L., 2005. Spatial and seasonal variations of nitrate-based new production and primary production in the South China Sea. Deep-Sea Research I 52, 319–340.

Chen, B., 2009. Distribution characteristics of the carbonate system in the southwestern Taiwan Strait and the air-sea CO_2 flux: the role of upwelling. Xiamen University. Master thesis.

Chen, J., 2011. Validation of Quik SCAT data and their application in the analysis of wind characteristics of Taiwan Strait and its adjacent waters in winter 2008. Journal of Oceanography in Taiwan Strait 30, 158–164 in Chinese with English abstract.

Chen, C.T.A., Huang, T.H., Chen, Y.C., Bai, Y., He, X., Kang, Y., 2013. Air-sea exchanges of CO_2 in the world's coastal seas. Biogeosciences 10, 6509–6544.

Chou, W.C., Gong, G.C., Sheu, D.D.D., Hung, C.C., Tseng, T.F., 2009. Surface distributions of carbon chemistry parameters in the East China Sea in summer 2007. J. Geophys. Res. Oceans 114, C07026.

Chou, W.C., Gong, G.C., Tseng, C.M., Sheu, D.D.D., Hung, C.C., Chang, L.P., Wang, L.W., 2011. The carbonate system in the East China Sea in winter. Mar. Chem. 123, 44–55.

Dai, M., Zhai, W., Cai, W.-J., Callahan, J., Huang, B., Shang, S., Huang, T., Li, X., Zhongming, Lu., Chen, W., Chen, Z., 2008. Effects of an estuarine plume-associated bloom on the carbonate system in the lower reaches of the Pearl River estuary and the coastal zone of the northern South China Sea. Cont. Shelf Res. 28 (12), 1416–1423.

Dai, M., Cao, Z., Guo, X., Zhai, W., Liu, Z., Yin, Z., Yanping, Xu., Gan, J., Jianyu, Hu., Chuanjun, Du., 2013. Why are some marginal seas sources of atmospheric CO_2? Geophys. Res. Lett. 40, 2154–2158.

Dai, M., Jianzhong, Su., Zhao, Y., Hofmann, E.E., Cao, Z., Cai, W.-J., Gan, J., Lacroix, F., Laruelle, G.G., Meng, F., Mueller, J.D., Regnier, P.A.G., Wang, G., Wang, Z., 2022. Carbon fluxes in the coastal ocean: Synthesis, boundary processes, and future Trends. Annu. Rev. Earth Planet. Sci. 50, 593–626.

Evans, W., Hales, B., Strutton, P.G., 2011. The seasonal cycle of surface ocean pCO_2 on the Oregon shelf. J. Geophys. Res. Oceans 116, C05012.

Guo, X., Zhai, W., Dai, M., Zhang, C., Bai, Y., Yi, Xu., Li, Q., Wang, G., 2015. Air-sea CO_2 fluxes in the East China Sea based on multiple-year underway observations. Biogeosciences 12 (18), 5123–5167.

Hales, B., Takahashi, T., Bandstra, L., 2005. Atmospheric CO_2 uptake by a coastal upwelling system. Global Biogeochem. Cycles 19 (1), GB1009.

Huang, B., Liu, C., Banzon, V., Freeman, E., Graham, G., Hankins, B., Smith, T., Zhang, H.-M., 2021. Improvements of the daily optimum interpolation sea surface temperature (DOISST) version 2.1. J. Clim. 34, 2923–2939.

Hu, J.Y., Kawamura, H., Hong, H.S., Pan, W.R., 2003. A review of research on the upwelling in the Taiwan Strait. Bull. Mar. Sci. 73 (3), 605–628.

Jiang, L.Q., Cai, W.-J., Wanninkhof, R., Wang, Y.C., Luger, H., 2008. Air-sea CO_2 fluxes on the US South Atlantic Bight: Spatial and seasonal variability. J. Geophys. Res. Oceans 113, C07019.

Jo, Y.H., Dai, M.H., Zhai, W.D., Yan, X.H., Shang, S.L., 2012. On the variations of sea surface pCO_2 in the northern South China Sea: A remote sensing based neural network approach. Journal of Geophysical Research: Oceans 117 (C08), C08022. https://doi.org/10.1029/2011JC007745.

Kim, D., Choi, S.H., Shim, J.H., Kim, K.H., Kim, C.H., 2013. Revisiting the seasonal variations of sea-air CO_2 fluxes in the northern East China Sea. Terrestrial Atmospheric Oceanic Sciences 24, 409–419.

Kuttippurath, J., Peter, R., Singh, A., Raj, S., 2022. The increasing atmospheric CO_2 over India: Comparison to global trends. iScience 25 (8), 104863.

Large, W.G., McWilliams, J.C., Doney, S.C., 1994. Oceanic vertical mixing: a review and a model with a nonlocal boundary layer parameterization. Rev. Geophys. 32 (4), 363–403.

Laruelle, G.G., Dürr, H.H., Slomp, C.P., Borges, A.V., 2010. Evaluation of sinks and sources of CO_2 in the global coastal ocean using a spatially-explicit typology of estuaries and continental shelves. Geophys. Res. Lett. 37, L15607.

Laruelle, G.G., Cai, W.-J., Hu, X., Gruber, N., Mackenzie, F.T., Regnier, P., 2018. Continental shelves as a variable but increasing global sink for atmospheric carbon dioxide. Nat. Commun. 9, 454.

Li, L.i., Guo, X., Risheng, Wu., 2000. Oceanic fronts in southern Taiwan Strait. Journal of Oceanography in Taiwan Strait 19 (2), 147–156 in Chinese with English abstract.

Li, Q., Guo, X., Zhai, W., Yi, Xu., Dai, M., 2020. Partial pressure of CO_2 and air-sea CO_2 fluxes in the South China Sea: Synthesis of an 18-year dataset. Prog. Oceanogr. 182, 102272.

Pan, A., Guo, X., Jindian, Xu., Huang, J., Wan, X., 2011. Responses of Guangdong coastal upwelling to the summertime typhoons of 2006. Sci. China Earth Sci. 55 (3), 495–506.

Peter, R., Kuttippurath, J., Sunanda, N., Chakraborty, K., 2025. Effect of thermal and non-thermal processes on the variability of ocean surface pCO_2 and buffering capacity in the north Indian Ocean. Prog. Oceanogr. 233, 103442.

Pierrot, D., Neill, C., Sullivan, K., Castle, R., Wanninkhof, R., Luger, H., Johannessen, T., Olsen, A., Feely, R.A., Cosca, C.E., 2009. Recommendations for autonomous underway pCO_2 measuring systems and data-reduction routines. Deep-Sea Res. II 56, 512–522.

Roobaert, A., Regnier, P., Landschützer, P., Laruelle, G.G., 2024. A novel sea surface pCO_2 product for the global coastal ocean resolving trends over 1982-2020. Earth Syst. Sci. Data 16 (1), 421–441.

Shim, J., Kim, D., Kang, Y.C., Lee, J.H., Jang, S.T., Kim, C.H., 2007. Seasonal variations in pCO_2 and its controlling factors in surface seawater of the northern East China Sea. Cont. Shelf Res. 27, 2623–2636.

Sweeney, C., Gloor, E., Jacobson, A.R., Key, R.M., McKinley, G., Sarmiento, J.L., Wanninkhof, R., 2007. Constraining global air-sea gas exchange for CO_2 with recent bomb ^{14}C measurements. Global Biogeochem. Cycles 21 (2), GB2015.

Takahashi, T., Olafsson, J., Goddard, J.G., Chipman, D.W., Sutherland, S.C., 1993. Seasonal variation of CO_2 and nutrients in the high latitude surface oceans-a comparative study. Global Biogeochem. Cycles 7 (4), 843–878.

Takahashi, T., Sutherland, S.C., Sweeney, C., Poisson, A., Metzl, N., Tilbrook, B., Bates, N., Wanninkhof, R., Feely, R.A., Sabine, C., Olafsson, J., Nojiri, Y., 2002. Global sea-air CO_2 flux based on climatological surface ocean pCO_2, and seasonal biological and temperature effects. Deep-Sea Res. II 49 (9–10), 1601–1622.

Takahashi, T., Sutherland, S.C., Wanninkhof, R., Sweeney, C., Feely, R.A., Chipman, D. W., Hales, B., Friederich, G., Chavez, F., Sabine, C., Watson, A., Bakker, D.C.E., Schuster, U., Metzl, N., Yoshikawa-Inoue, H., Ishii, M., Midorikawa, T., Nojiri, Y., Kortzinger, A., Steinhoff, T., Hoppema, M., Olafsson, J., Arnarson, T.S., Tilbrook, B., Johannessen, T., Olsen, A., Bellerby, R., Wong, C.S., Delille, B., Bates, N.R., de Baar, H.J.W., 2009. Climatological mean and decadal change in surface ocean pCO_2, and net sea-air CO_2 flux over the global oceans. Deep-Sea Research II 56, 554–577.

Thomas, H., Bozec, Y., Elkalay, K., Baar, H.J.W.D., 2004. Enhanced open ocean storage of CO_2 from shelf sea pumping. Science 304, 1005–1008.

Tseng, C.M., Liu, K.K., Gong, G.C., Shen, P.Y., Cai, W.-J., 2011. CO_2 uptake in the East China Sea relying on Changjiang runoff is prone to change. Geophys. Res. Lett. 38, L24609.

Tsunogai, S., Watanabe, S., Nakamura, J., Ono, T., Sato, T., 1997. A preliminary study of carbon system in the East China Sea. J. Oceanogr. 53, 9–17.

Tsunogai, S., Watanabe, S., Sato, T., 1999. Is there a "continental shelf pump" for the absorption of atmospheric CO_2? Tellus B: Chem. Phys. Meteorol. 51 (3), 701–712.

Wanninkhof, R., 1992. Relationship between wind speed and gas exchange over the ocean. J. Geophys. Res. Oceans 97 (C5), 7373–7382.

Wanninkhof, R., Doney, S.C., Takahashi, T., McGillis, W.R., 2002. The effect of using time-averaged winds on regional air-sea CO_2 fluxes. Geophys. Monogr. Ser. 127, 351–357.
Weiss, R.F., 1974. Carbon dioxide in water and seawater: the solubility of a non-ideal gas. Mar. Chem. 2 (3), 203–215.
Weiss, R.F., Price, B.A., 1980. Nitrous oxide solubility in water and seawater. Mar. Chem. 8 (4), 347–359.
Yang, W., Guo, X., Cao, Z., Yi, Xu., Dai, M., 2021. Seasonal dynamics of the carbonate system under complex circulation schemes on a large continental shelf: the northern South China Sea. Prog. Oceanogr. 197 (12), 102630.
Zhai, W., Dai, M., 2009. On the seasonal variation of air-sea CO_2 fluxes in the outer Changjiang (Yangtze River) Estuary. East China Sea. Marine Chemistry 117, 2–10.
Zhai, W., Dai, M., Cai, W.-J., Wang, Y., Hong, H., 2005. The partial pressure of carbon dioxide and air-sea fluxes in the northern South China Sea in spring, summer and autumn. Mar. Chem. 96 (1–2), 87–97.
Zhai, W., Dai, M., Chen, B., Guo, X., Li, Q., Shang, S., Zhang, C., Cai, W.-J., Wang, D., 2013. Seasonal variations of sea-air CO_2 fluxes in the largest tropical marginal sea (South China Sea) based on multiple-year underway measurements. Biogeosciences 10 (11), 7775–7791.
Zhai, W., Guo, X., Bai, Y., He, X., Tang, K., Dai, M., 2025. Surface CO_2 partial pressure and air-sea CO_2 flux on the China side of the South Yellow Sea based on multiple-year underway measurements during 2005-2011 and comparison with results for 2011-2018. Prog. Oceanogr. 234, 103466.